Journal of
Materials Chemistry A

ROYAL SOCIETY
OF CHEMISTRY

REVIEW

View Article Online
View Journal | View Issue

Check for updates

Cite this: *J. Mater. Chem. A*, 2017, **5**, 17676

Recent progress in nanostructured silver sulfide: from synthesis and nonstoichiometry to properties

S. I. Sadovnikov* and A. I. Gusev*

Received 7th June 2017
Accepted 24th July 2017

DOI: 10.1039/c7ta04949h

rsc.li/materials-a

The microstructure (composition, nonstoichiometry, size and shape of particles) of nanostructured semiconductor silver sulfide (Ag_2S) determines its electronic structure, optical and electrical properties, and possible applications of Ag_2S in modern electronics, biology and medicine. This critical review summarizes recent progress in the design of different forms of nanostructured Ag_2S from nanopowders to colloidal solutions, quantum dots and heteronanostructures. Main results on the synthesis, structural features and properties of nanostructured Ag_2S are detailed. The appearance of nonstoichiometry in silver sublattices of monoclinic Ag_2S at decreasing size particles to the nanometer scale is considered. The interdependent changes in nonstoichiometry and crystal structure at the transformation of a nonconducting nanocrystalline Ag_2S in superionic conductors are discussed. The effects of nanocrystalline state on the peculiarities of crystal structure, nonstoichiometry, optical and thermal properties of semiconductor Ag_2S are considered. Special attention is paid to manifold applications of Ag_2S-based nanomaterials and heteronanostructures in biomarkers, resistance-switches and nonvolatile memory devices.

1. Introduction

The synthesis and properties of nanostructured chalcogenides, including semiconducting lead sulfide (PbS), cadmium sulfide (CdS), mercury sulfide (HgS), copper(II) sulfide (CuS), Cu_2S, and

Institute of Solid State Chemistry, Ural Branch of the Russian Academy of Sciences, 620990 Ekaterinburg, Russia. E-mail: sadovnikov@ihim.uran.ru; gusev@ihim.uran.ru

Dr Stanislav I. Sadovnikov graduated in the materials science of semiconductors from the Ural State Technical University, Russia. He is currently a Senior Research Scientist at the Laboratory of Nonstoichiometric Compounds in the Institute of Solid State Chemistry of the Ural Branch of the Russian Academy of Sciences. He has studied the synthesis, structure and properties of nanostructured semiconducting sulfides for more than 10 years. He is mostly recognized as an expert in the field of nanosized sulfide synthesis. He is an author of two review articles, more than 60 scientific articles, and seven patents on nanostructured lead and silver sulfides. His current research interests are focused on the development of new methods of synthesis of semiconductor heteronanostructures for optoelectronics, photocatalysis and biosensing.

Professor Dr Aleksandr I. Gusev graduated in physical chemistry from the Ural State Technical University, Russia. He is Chief Research Scientist at the Laboratory of Nonstoichiometric Compounds in the Institute of Solid State Chemistry of the Ural Branch of the Russian Academy of Sciences. He has been exploring crystal and electronic structures and the properties of novel nonstoichiometric compounds such as carbides, sulfides, and oxides, and nanostructured advanced materials for more than 40 years. He is an author of 16 monographs including Disorder and Order in Strongly Nonstoichiometric Compounds (Springer, 2001), Nanocrystalline Materials (Cambridge, 2004), and Tungsten Carbides: Structure, Properties and Application in Hardmetals (Springer, 2013), 23 review articles and more than 350 scientific articles. His current interests lie in the materials science of nanostructured semiconductor sulfides.

silver sulfide (Ag_2S), have been described in a number of review articles and books.[1–10] However, too broad range of objects inevitably made the discussion too compact. Nanostructured Ag_2S has been mentioned in these works very briefly. Nonstoichiometry (*i.e.*, deviation from stoichiometric composition) of Ag_2S has not been considered at all.

Nonstoichiometry is a fundamental characteristic of inorganic substances, which affects the structure and properties of compounds, on the one hand, and depends on the size of structural elements (particles, grains, crystallites, domains) of compounds, on the other hand. Until recently, the relationship and interdependence between nonstoichiometry and particle size at the nanometer scale has been scarcely examined or discussed only as an example of strongly nonstoichiometric compounds (*e.g.*, carbides, oxides, nitrides of transition metals). Certainly the nonstoichiometry in nanostructured sulfides, which in the conventional bulk (coarse-grained) state are traditionally considered to be stoichiometric compounds, has never been discussed. Indeed, at present the number of studies devoted to nonstoichiometry of sulfide nanoparticles is extremely limited.

Modern solid-state physics, physical material science and electronics are inconceivable without semiconducting heterostructures. Such semiconducting heterostructures as quantum wells, quantum wires and quantum dots allow control of fundamental parameters of semiconducting crystals as the forbidden band width, effective mass and mobility of charge carriers and electronic energy spectrum.[6,11–13] Heteronanostructures combining the properties of semiconductors in the nanocrystalline state, on the one hand, and nonstoichiometry, on the other hand, are the next step in the development of quantum electronics.

We have tried to take into account both the purely scientific, fundamental interest in the problem of nanostructured Ag_2S and some applied aspects of this problem that are of considerable importance for practical application of Ag_2S.

The well-known Ag_2S is one of the most requisite semiconducting sulfides[1,2,14–19] along with lead, zinc, cadmium and copper sulfides.[3–5,20–25]

Ag_2S is the only semiconducting sulfide (except for HgS) having three polymorphous modifications (α-Ag_2S, β-Ag_2S and γ-Ag_2S) within rather close temperature intervals.[26] These modifications of Ag_2S differ greatly in their structure and properties. The unique character of Ag_2S has to do also with the transition between semiconducting α-Ag_2S and superionic β-Ag_2S phases. The presence of this transformation makes it possible to use Ag_2S in Ag_2S/Ag heteronanostructures intended for new-generation microelectronic devices such as resistance nanoswitches and nonvolatile memory nanodevices.

Low-temperature semiconducting-phase α-Ag_2S (acanthite) with monoclinic crystal structure exists at temperatures below ~450 K. Under equilibrium conditions, cubic phase β-Ag_2S (argentite) exists in the temperature range 452–859 K, has a body centered cubic (bcc) sublattice of sulfur (S) atoms and has a superionic conductivity. High-temperature cubic γ-Ag_2S phase with a face centered cubic (fcc) sublattice of S atoms is stable from ~860 K up to melting temperature.

It is thought that the monoclinic α-Ag_2S phase is stoichiometric, whereas cubic β-$Ag_{2\pm\delta}$ S and γ-$Ag_{2\pm\delta}$ S with $\delta \cong 0.002$ are nonstoichiometric phases having either a small deficiency or small excess of silver. The homogeneity intervals of cubic allotropic forms of Ag_2S have been determined.[27–33] According to,[34] nonstoichiometric body centered cubic β-$Ag_{2+\delta}$ S ($\delta \leq 0.002$) is characterized by high electronic conductivity of about $1.3 \times 10^3\ \Omega^{-1}\ \mathrm{cm}^{-1}$ that is 10^6 times higher than that in the monoclinic α-Ag_2S phase. Owing to high electronic conductivity, bcc β-Ag_2S can be used in photography.[34]

In normal conditions, bulk coarse-crystalline Ag_2S with an α-Ag_2S acanthite-type structure is a direct semiconductor which possesses a wide band gap E_g and low charge-carrier mobility. The band gap E_g of α-Ag_2S depends on temperature. According to,[35,36] the band gap of acanthite α-Ag_2S at 300 K is about 0.9 eV, and its temperature coefficient $\partial E_g/\partial T = -(1.2 - 1.5) \times 10^{-3}\ \mathrm{eV\ K^{-1}}$.[36] The conventional band gap of acanthite α-Ag_2S at 300 K is 0.9–1.1 eV.

For bulk coarse-crystalline acanthite α-Ag_2S, the electron and hole effective masses are $m_e = 0.286m_0$ and $m_h = 1.096m_0$, respectively.[37] Taking this into account, the reduced exciton mass $\mu_{ex} = m_e m_h/(m_e + m_h)$ for acanthite α-Ag_2S is $\sim 0.23m_0 = 2.06 \times 10^{-31}$ kg.

The characteristic size of the Wannier–Mott exciton (or the Bohr radius of the exciton) in the macroscopic (bulk) semiconductor has been determined to be

$$R_{ex} \approx n^2\hbar^2\varepsilon/\mu_{ex}e^2 = (n^2\varepsilon m_0/\mu_{ex})a_B, \tag{1}$$

where $a_B = \hbar^2/m_0e^2 = 0.0529$ nm is the Bohr radius. For reduced exciton mass $\mu_{ex} = 0.23m_0$ and dielectric constant $\varepsilon = 5.95$,[38] the radius R_{ex} of the first exciton state with $n = 1$ in coarse-crystalline acanthite α-Ag_2S is equal to $(26 \pm 1)a_B$ or $\sim 1.4 \pm 0.1$ nm and the exciton diameter D_{ex} is about 2.8 nm.

2. Methods of synthesis of nanostructured Ag_2S

Nanostructured Ag_2S has been investigated intensively in recent years due to possible application in optoelectronics, biosensing and catalysis.[39–42] It is an excellent substance for the preparation of heterostructures.[43] Nanostructured Ag_2S can be used in photochemical cells,[44] infrared detectors,[45–47] in resistance-switches and nonvolatile memory devices.[48–50] Ag_2S is a promising material for conversion of solar energy into electrical energy.[51,52] Recently, three-dimensional nanoparticle superlattices were built up with Ag_2S hollow nanospheres and nanodiscs as building blocks.[53] Ag_2S nanoparticles possess antibacterial action.[54,55] Creation of isolated, stable Ag_2S quantum dots to be used as biomarkers holds much promise.[56,57]

Nanostructured silver chalcogenides including Ag_2S also have been showing promising applications in thermoelectrics.[58] The thermoelectric effect refers to phenomena by which either a temperature difference creates an electric potential or an electric potential creates a temperature difference. The dimensionless figure of merit (thermoelectric performance) *ZT* of any material is determined as $\sigma S^2T/\kappa$, where σ is the electrical conductivity, S is the Seebeck coefficient, κ is the thermal conductivity of the material, and T is the absolute temperature. Tellurides, selenides, sulfides, and their solid solutions are the most attractive thermoelectric materials.[58–61] Silver chalcogenides Ag_2Se and Ag_2S have attracted much interest due to reversible transformation between semiconductor and superionic phases. In study,[58] it has been shown that the Seebeck coefficient and ZT for Ag_2S nanocrystal are equal to $-76\ \mu V\ K^{-1}$ and 0.12 at the temperature of the transition from α-Ag_2S to β-Ag_2S. For nanocrystalline Ag_2Se and Ag_4SeS, values of ZT are 0.23 and 0.33, respectively. According to,[60] the Seebeck coefficient of Ag_2S nanocrystalline film is $-198\ \mu V\ K^{-1}$ at 400 K; therefore, enhanced ZT for Ag_2S nanofilms can be anticipated. According to,[58] the cooperative contribution of superionic phase transition, reduced grain size, and alloying opens up a promising new approach to "tailor" sulfide materials for optimal thermoelectric performance.

Nanostructured Ag_2S in the form of nanopowders, quantum dots, and heteronanostructures based on Ag_2S has been successfully produced by different methods such as hydrochemical deposition, template method, sol–gel method, synthesis in microemulsions, as well as by sonochemical, hydrothermal, solvothermal, electrochemical, microwave and other techniques. Every method has both advantages and limitations.

Sodium sulfide (Na_2S)[30,40,62–68] hydrogen sulfide gas or hydrosulfuric acid (H_2S),[69] elemental S dissolved in a concentrated NaOH solution,[70] solution of toxic carbon disulfide (CS_2) in ethanol,[71–74] sodium thiosulfate ($Na_2S_2O_3$),[75] a solution of 3-thiopropionic-(3-mercaptopropionic) acid ($C_3H_6O_2S$) in ethylene glycol (EG) as solvent,[56] thiocarbamide (N_2H_4CS),[52,53,76,77] and thioacetamide ($CH_3C(S)NH_2$)[78] and their derivatives are used for sulfidizing the soluble complex compounds of Ag and other metals.

Recently, much attention has been devoted to the production of different hybrid heteronanostructures of the core–shell type, which include Ag and its compounds ($Ag_2O@Ag_2S$, $Ag@SiO_2$, *etc.*).[79–81] In particular, familiar core–shell nanostructures can be formed by two different semiconductors (CdSe@CdS, CdSe@ZnS, $CdS@Ag_2S$, CdS@ZnS, GaAs@AlS, *etc.*).[82–86]

The nanosized particles are not stable. The high surface energy will impel the nanoparticles to aggregate. Therefore, creation of core–shell particles can be due to the necessity of fixing of specific groups (organic ligands) on the surface of the core, which would prevent agglomeration, growth, and oxidation of particles and provide the production of stable isolated nanoparticles. Using the protective shell, it is possible to control the size of isolated nanoparticles. Stabilizing and capping agents such as trioctylphosphine oxide,[87,88] L-cysteine,[89–91] glutathione,[92] long-chain amines (hexadecylamine, octylamine, dioctylamine, ethylenediamine),[39] ethylenediaminetetraacetic acid (EDTA) and EG[75,93] are used for the creation of a protective shell. However, most of the listed stabilizing agents are hazardous to human health and have a serious impact on the environment. One of the most commonly requested non-toxic capping agents which has a high degree of electrostatic stabilization is sodium citrate ($Na_3C_6H_5O_7 \equiv Na_3Cit$).[55,68,69,94–96]

Several investigations[97–100] have shown that extracts or aqueous solutions of natural products (leaves, seeds, fruits, roots, honey, royal jelly, gum of trees, bovine serum albumin, *etc.*) can be used as stabilizing agents for the preparation of isolated nanoparticles of Ag_2S and Ag with a protective shell. Such exotic stabilizing agents are non-toxic and do not exert a harmful impact on the environment due to their high antioxidant potential. However, the complete identification of the complex composition of listed natural stabilizing agents has been an open and undecided problem until now. Therefore, real application of natural stabilizing agents is rather limited.

The most pronounced part in the formation of Ag_2S nanoparticles has been played by complexing agents. Na_3Cit is the main complexing agent for Ag^+. One must point out that the Na_3Cit is the completely harmless standardized food additive E331.

2.1 Synthesis by decomposition of molecular precursors

Application of molecular precursors has some attractive features. On the one hand, it provides such important advantages as simplicity, safety and compatibility with metal organic chemical vapor deposition.[101] On the other hand, the use of molecular precursors may lead to the unusual selectivity in crystal growth or formation of the metastable phase of the final products, which are not always achievable by conventional synthetic methods.

Among the solution methods, the injection of an organometallic precursor into a hot solvent provides a simple route to produce particles with desirable properties (*e.g.*, high crystallinity, and uniform shapes and sizes with a high degree of monodispersity).

Lim *et al.*[39] discovered that air-stable precursors such as silver thiobenzoate (Ag(SCOPh)) meets these requirements. The precursor crystals were found to decompose in amine at room temperature to give Ag_2S nanoparticles. The most important parameters of synthesis are the reaction temperature, type of amine, relative concentration of the reagents, and reaction time. Lim *et al.*[39] found that by increasing the injection temperature to 393 K, cube-shaped Ag_2S nanocrystals are obtained exclusively (Fig. 1). The uniform Ag_2S nanocubes self-assemble into ordered two-dimensional arrays on the surface of the transmission electron microscope grid (Fig. 1a). The average size of these nanocubes is 44 ± 4 nm. The scanning electron microscopy (SEM) image in Fig. 1b illustrates that large quantity of these nanocubes can be obtained using this approach. High-resolution transmission electron microscopy (HRTEM) images (Fig. 1c and d) clearly show that Ag_2S nanocubes are single crystals.

Later, spherical Ag_2S nanocrystals were obtained *via* a modified hot-injection process of the same single-source molecular precursor Ag(SCOPh), which can potentially generate both Ag* and AgS* fragments simultaneously.[102] Wang *et al.*[103] obtained Ag_2S nanocrystallites by heating molecular precursors such as silver diethyldithiocarbamate (Ag–DDTC) in air at 473 K for 3 h, and used this air-stable molecular precursor

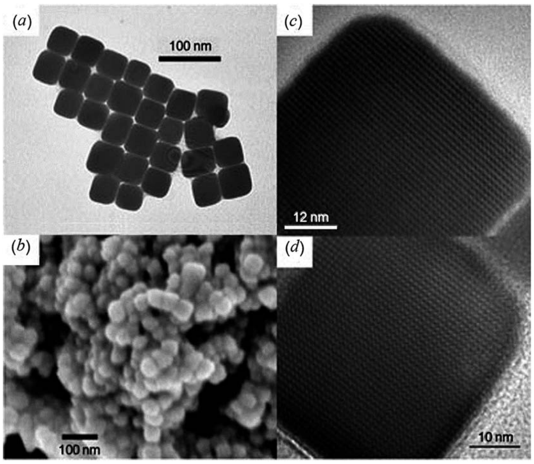

Fig. 1 Ag_2S nanocubes produced at 393 K:[39] (a) TEM image of Ag_2S nanocubes; (b) SEM image of clusters formed by Ag_2S nanocubes; (c) and (d) HRTEM images of Ag_2S nanocubes. Reproduced from ref. 139 with permission from Wiley.

as the reactant source. The proposed method was both cost-effective and non-toxic. Monodisperse Ag_2S nanoparticles with controlled size were successfully synthesized by thermolysis of harmless silver xanthates as a single-source molecular precursor.[104] In one experiment,[104] the diameter of the Ag_2S nanoparticles ranged from 8.9 ± 1.2 nm to 48 ± 4 nm (Fig. 2). Control of the particle size has been achieved by simply changing the alkyl chain length in the precursors.

2.2 Synthesis of nanostructured Ag_2S with different morphology

Recently, great efforts have been focused on the preparation of Ag_2S nanoparticles of various morphology, and on the morphology control of the semiconductor nanocrystals.[105] For example, Zhao *et al.*[106] prepared rod-like Ag_2S nanocrystals using $Na_2S_2O_3$ as a S source *via* gamma-ray irradiation of aqueous solutions at room temperature.

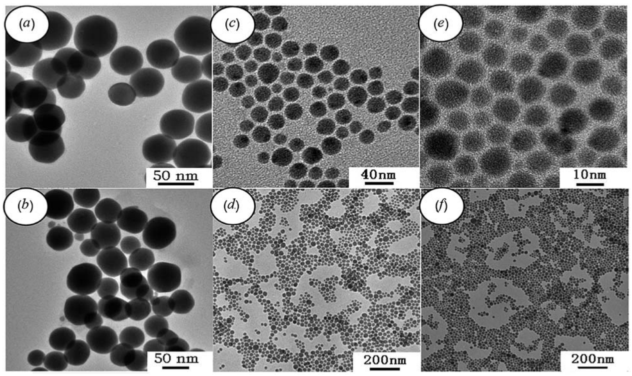

Fig. 2 TEM images of Ag_2S nanoparticles synthesized by solvent-less thermolysis of (a and b) silver octyl xanthate, (c and d) silver hexadecyl xanthate, and (e and f) silver carnaubyl xanthate. Reprinted from ref. 104 with permission from Elsevier.

An alcohol solution method to synthesize nanostructured Ag_2S using carbon bisulfide (CS_2) as the S source has been described.[107] All the products were irregular Ag_2S microstructures and nanostructures. When the reaction medium was changed from water and alcohol–water to alcohol, the morphology of synthesized Ag_2S changed from big irregular nanosheets to leaf-like nanosheets, elliptical, and Y-shaped flaked Ag_2S nanoparticles.

Later, Chen *et al.*[108] reported that leaf-like Ag_2S nanosheets were prepared successfully by a facile hydrothermal method from a mixture of alcoholic CS_2 solution with an aqueous solution of $AgNO_3$ and NH_3.

Ag_2S microstructures and nanostructures with different morphologies, including micrometer bars, nanowires, and nanopolyhedrons, have been synthesized by a facile one-step method at room temperature.[109] In the proposed method, no organic template materials were added to the reaction mixture, which contained aqueous solutions of $AgNO_3$, NH_3, and N_2H_4CS. By changing the reactant concentration ratio, the size and morphology of prepared Ag_2S particles can be easily tuned.

In recent years, polyhedral nanocrystals, including face-centered cubic sulfide nanocrystals,[39,110] have been successfully fabricated. Wang *et al.*[110] prepared Ag_2S nanocrystals by thermolysis of an organometallic precursor $Ag[S_2P(OR)_2]$ ($R = C_nH_{2n+1}$). The above-mentioned hydrothermal method has been improved by Dong *et al.*[111] Most of the observed Ag_2S nanoparticles looked hexagonal.

Ag_2S-poly(*N*-isopropylacrylamide-*co*-methacrylic acid) (PNIPAM–MAA) and Ag_2S–PNIPAM composite microspheres with patterned surface structures have been synthesized by a polymeric minigel template method.[112] The surface structure of Ag_2S–PNIPAM–MAA microspheres looks like flowers.

Single-crystalline Ag_2S hollow nanohexagons with narrow size distribution were successfully synthesized in aqueous solutions of $AgNO_3$, $N_2S_2O_3$, and $C_{19}H_{42}BrN$ (CTAB) at 318 K.[113]

Tetrahedral colloidal crystals of Ag_2S nanoparticles have been synthesized from aqueous solutions of $AgNO_3$, NH_3, and 1-dodecanethiol ($CH_3(CH_2)_{11}SH$) in an autoclave at 473 K for 5 h.[114] Due to the high uniformity and van der Waals interactions, Ag_2S nanoparticles spontaneously assemble into tetrahedral colloidal aggregates comprising a perfectly ordered 3D superlattice structure (Fig. 3).

A sacrificial core of S nanoparticles is used to synthesize Ag_2S hollow nanospheres *via* a wet chemical method at room temperature.[115] S nanoparticles as cores were synthesized from $Na_2S_2O_3$ in the presence of cetyltrimethyl ammonium bromide aqueous solution. After completion of the formation of cores, the $AgNO_3$ solution was added. Then, the produced particles were washed by a water–ethanol mixture and treated with CS_2 for the complete conversion of AgBr to Ag_2S, as well as to remove the cores to form Ag_2S hollow nanospheres (Fig. 4).

Worm-like Ag_2S nanofibers with lengths up to several micrometers and diameters of 25–50 nm have been prepared in reverse microemulsions in the presence of $CH_3C(S)NH_2$ as a S source and EDTA as a chelating ligand.[116]

In study,[117] rice-shaped Ag_2S nanoparticles were produced by the reaction between $Ag(NH_3)_2^+$ and Na_2S in the presence of

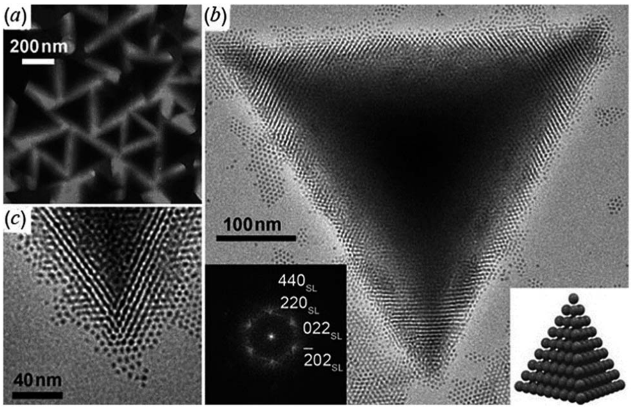

Fig. 3 Ag_2S tetrahedral superlattice colloidal crystals:[114] (a) TEM image at low magnification; (b) a typical HRTEM image of an individual tetrahedron at high magnification; the left inset is the diffraction pattern calculated using fast Fourier transform (FFT) of HRTEM images and the right inset is a scheme of the tetrahedral superlattice colloidal crystal; (c) magnified TEM image of a vertex of the tetrahedron. Reproduced from ref. 114 with permission from Wiley.

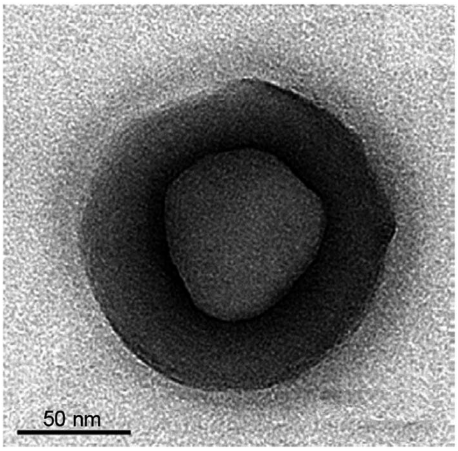

Fig. 4 TEM image of a hollow Ag_2S particle synthesized from a reaction mixture of silver nitrate and thiosulfate. Reprinted from ref. 115 with permission from Elsevier.

polyvinylpyrrolidone $(C_6H_9NO)_n$ (PVP) through a hydrothermal method.

Large, rice-shaped Ag_2S particles have been synthesized by hydrochemical bath deposition from aqueous reaction mixture of silver nitrate ($AgNO_3$), Na_2S, and Na_3Cit.[118] Reaction mixture was heated in closed vessel at a temperature of 373 K under the pressure $\sim 2 \times 10^5$ Pa within 2 h.

2.3 Synthesis of Ag_2S nanowires

The one-dimensional (1D) nature of Ag_2S nanowires endows their unique electrical, optoelectronic, and mechanical properties. Single-crystalline Ag_2S nanowires can be expected to have superior properties owing to their anisotropic geometry, and carrier and photon confinement in two dimensions. Conventional nanowire synthesis often requires high temperature and/or various templates.

According to,[119,120] there are two different routes for the synthesis of 1D nanomaterials, namely, "hard" and "soft" approaches. The first approach includes template-directed synthesis and the vapor–liquid–solid and vapor–solid techniques, which usually require high temperature and pressure. In comparison, the soft approaches, such as hydrothermal/solvothermal processes, the solution–liquid–solid mechanism, and capping agents/surfactant-assisted synthesis, provide a convenient and low-temperature pathway for the fabrication of 1D nanomaterials.

Recently, Ag_2S nanowires have been synthesized through the gas–solid reaction route,[121] anodic aluminum oxide template method,[122] microwave irradiation-assisted method,[123] and hydrothermal method with amine ligand.[120]

Wen *et al.*[121] reported on the successful synthesis of Ag_2S nanowires by a simple and mild gas–solid reaction method on Ag substrates. For the nanowire synthesis, the cleaned Ag foil was subjected to preoxidation and sulfidizing by an exposition in an atmosphere of an O_2/H_2S mixture from room temperature to 313 K in a water bath. The resulting Ag_2S nanowires contained one-phase monoclinic acanthite α-Ag_2S and had diameter of 40–150 nm and lengths up to 100 μm.

In other syntheses,[120] $AgNO_3$ was dissolved in warm octadecylamine solvent, forming silver ammines that were rapidly converted to Ag_2S nuclei upon the addition of S powder. After stirring, the system was maintained at 393 K for further growth and crystallization. This process resulted in the generation of ultralong Ag_2S nanowires with diameters in the range of 10–30 nm and lengths up to hundreds of micrometers. Authors[120] could only obtain uniform nanowires at a temperature neither lower nor higher than 393 K. Synthesized Ag_2S nanowires are very sensitive to oxygen and there is a quasi-linear ratio between the current and the logarithm of oxygen pressure. These excellent performances indicate that Ag_2S nanowires are promising candidates for photoswitches and room-temperature oxygen sensors.

In work,[124] Ag_2S nanowires were prepared in anhydrous ethanol through a simple and sacrificial templating solvothermal route. The experimental results[124] demonstrated that the reaction temperature, Ag^+ concentration, reaction time and solvent played crucial parts in the formation of the Ag_2S nanowires. In a typical procedure, a mixture of S powder and $Cd(CH_3COO)_2$ were dissolved consecutively in ethylenediamine. The resulting mixture was heated in the autoclave at 473 K for 2 h. Then, as-prepared CdS nanowires and $AgNO_3$ were dissolved in anhydrous ethanol. The resulting mixture was heated in the autoclave at 473 K for 12 h. The addition of excess Ag^+ leads to the complete transformation of CdS nanowires to the Ag_2S nanowires.

Later,[125] a cation-exchange process was used for fabrication of Ag_2S nanowires. Authors[125] reported a sequential two-step cation exchange process which transformed single-crystal nanowires to twinning nanowires. Specifically, CdS nanowires were used as a template to form CdS–Cu_2S core shell nanowires and subsequently twinning Cu_2S nanowires through cation exchange. Then, twinning Cu_2S nanowires were transformed to Cu_2S–Ag_2S superlattice nanowires with tunable segment lengths *via* further cation exchange of Cu^+ by Ag^+. Fig. 5 shows the schematic synthetic sequence to form Cu_2S–Ag_2S superlattice nanowires from CdS nanowires. Thus, authors[125] have demonstrated that twins created in the cation exchange process of nanowires can be utilized to generate heterostructures in the chain cation exchange steps.

2.4 Preparing Ag_2S nanoparticles and quantum dots

Ag_2S quantum dots are treated as an ideal optical probe with fluorescence emission from UV to NIR region because these quantum dots have lower toxicity compared with chalcogenide quantum dots of such heavy metals as Pb, Ca, and Hg.[126,127] The synthesis of quantum dots, which can be used as optical probes for *in vitro* and *in vivo* molecular imaging, has made great progress.[128] The first synthesis of Ag_2S quantum dots with emission in the NIR-II region was demonstrated by Du and coauthors.[127] In a typical reaction, Ag–DDTC was mixed with oleic acid ($CH_3(CH_2)_7CH{=}CH(CH_2)_7COOH$), 1-octadecane ($CH_3(CH_2)_{16}CH_3$) and octadecylamine ($CH_3(CH_2)_{17}NH_2$).

In study,[129] highly monodisperse and water-soluble clusters representing Ag_2S quantum dots, covered by ribonuclease-A, were synthesized in aqueous medium *via* a biomimetic route (*i.e.*, by a method that mimics biochemical processes).

Siva *et al.*[130] noted that the biomolecules assisted the formation of inorganic nanostructures, facilitated electrostatic stabilization, and improved the optical properties of nanoparticles. In study,[130] aqueous solutions of $AgNO_3$ and aurochloric acid ($HAuCl_4$) and also a solution of L-cysteine in a mixture of water, ethylene glycol, and ethanol were used for synthesis of L-cysteine-capped Ag_2S and Ag_3AuS_2 nanocrystals. Ag_2S nanocrystals were prepared using Ag nuclei as a core. Siva *et al.*[130] proposed the following scheme of formation of Ag_2S particles:

$$Ag^+ + \text{L-cysteine} \xrightarrow{298\ \text{K}} [\text{Ag(L-cysteine)}_n]^+, \tag{2a}$$

$$[\text{Ag(L-cysteine)}^n]^+ + OH^- \xrightarrow{\text{ethanol decomposition, 343 K}} \text{L-cysteine-capped Ag}, \tag{2b}$$

$$\text{L-Cysteine capped Ag} \xrightarrow{\text{C–S bond rupture, 343 K}} Ag_2S. \tag{2c}$$

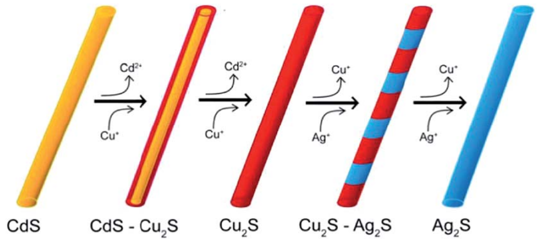

Fig. 5 Chain cation exchange process for the formation of a Cu_2S–Ag_2S superlattice NWs. Reprinted from ref. 125 with permission from ACS.

There are many other methods for synthesis of nanostructured Ag_2S. In study,[131] Ag_2S nanoparticles were prepared by pyrolysis using $AgNO_3$ and S powder as precursors, and oleylamine $C_{18}H_{35}NH_2$ as a solvent. Oleylamine acts as both a reducing agent and stabilizer during the synthesis. Ag_2S nanoparticles of uniform size were prepared by controlling the ratio amounts of $AgNO_3$: S and ripening time.

Shakouri-Arani and Salavati-Niasari[132] produced Ag_2S nanoparticles by a solvothermal process *via* reaction of $AgNO_3$ and a new sulfuring agent from the class of thio Schiff-base (2-(benzylidene amino)benzenethiol $C_{13}H_{11}NS$) in the presence of various solvents.

Nanostructured Ag_2S was obtained in the absence of a surfactant or presence of an anionic surfactant such as sodium dodecyl sulfate ($C_{12}H_{25}SO_4Na$; SDS) or such cationic surfactants as CTAB and polyethylene glycol (PEG) 20 000$C_{2n}H_{4n+2}O_{n+1}$ (HO–$(C_2H_4O)_n$–H). Surfactants were dissolved in solvents such as H_2O and 1-butanol C_4H_9OH.

Experimental results[132] indicate that the reaction temperature, presence of surfactant, and type of solvent affect the size of Ag_2S nanoparticles. Fig. 6 illustrates the influence of various conditions of synthesis on the formation of Ag_2S nanoparticles.

An improved hydrothermal/solvothermal method has been developed by Wang *et al.*[133] to prepare nanostructured Ag_2S. Using a liquid–solid–solution (LSS) system consisting of an ethanol–linoleic acid liquid phase, solid metal linoleate, and a water–ethanol solution under hydrothermal conditions, monodisperse Ag_2S nanocrystals of size 7.3 nm were successfully synthesized.

Biocompatible Ag_2S quantum dots were prepared through thermal decomposition of a single-source precursor, Ag–DDTC with $CH_3(CH_2)_{11}SH$ as a covalent ligand and solvent.[134] The reaction mixture was heated to 483 K at a heating rate of 15 K min^{-1} and kept for 1 h under a N_2 atmosphere. As a result, hydrophobic Ag_2S quantum dots with an average diameter from 5.4 to 10.0 nm coated with $CH_3(CH_2)_{11}SH$ as the surface ligand were obtained.

Stable and highly luminescent near-IR emitting Ag_2S colloidal quantum dots were prepared by a simple aqueous method using 2-mercaptopropionic acid ($C_3H_6O_2S$; 2-MPA) as a coating.[135] Nanoparticle size can be tuned between 2.3 and 3.1 nm with an emission maximum between 780 and 950 nm.

A similar one-step method was reported by Jiang *et al.*[56] using 3-mercaptopropionic acid (3-MPA) and EG rather than 2-MPA. In this case, the quantum dot surface was terminated with carboxyl groups. The PL emission wavelength of Ag_2S quantum dots was broadly tunable, from 510 to 1221 nm, by varying the growth time. Li *et al.*[57] demonstrated that Ag_2S quantum dots can be used as NIR luminescent probes for *in vivo* monitoring of lymphatic and vascular networks with deep penetration. They reported that Ag_2S quantum dots can provide spatial resolution of 40 μm during *in vivo* photoluminescence (PL) imaging, and this allowed them to monitor angiogenesis.

2.5 Hydrochemical deposition of different forms of nanostructured Ag_2S

Chemical deposition from aqueous solutions (also termed "chemical condensation method", and one-pot synthesis in

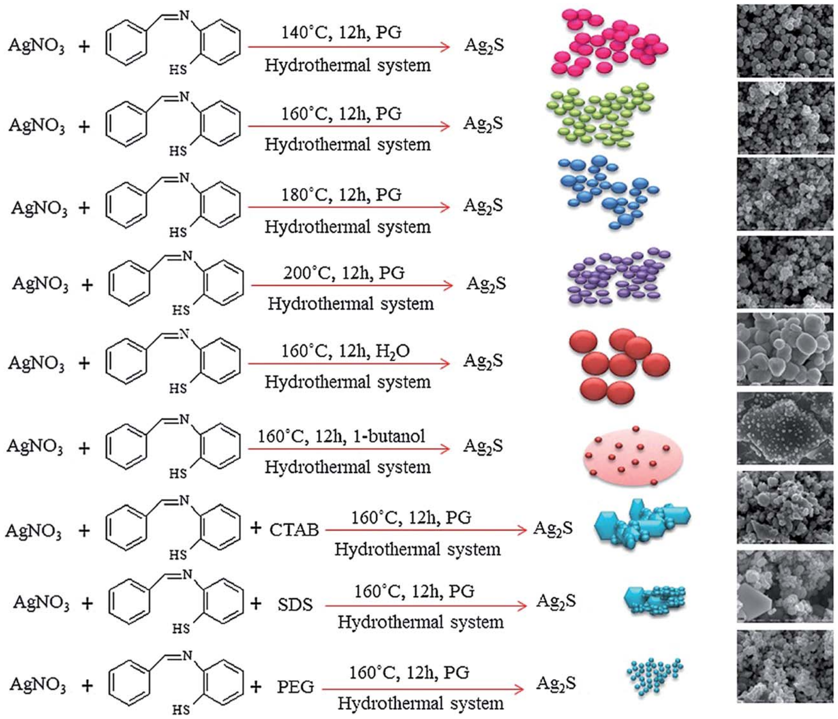

Fig. 6 Formation of Ag_2S nanoparticles at various conditions (schematic) (PG is propylene glycol ($C_3H_8O_2$), CTAB is cetyltrimethyl ammonium bromide ($C_{19}H_{42}BrN$), SDS is sodium dodecyl sulfate ($C_{12}H_{25}SO_4Na$) and PEG is polyethylene glycol 20 000 $C_{2n}H_{4n+2}O_{n+1}$). Reprinted from ref. 132 with permission from Elsevier.

aqueous solutions) and hydrochemical bath deposition are the most popular methods used for the synthesis of nanocrystalline sulfide powders.

Hydrochemical bath deposition is a well-known method which allows preparation of colloidal solutions of Ag_2S nanoparticles and quantum dots, nanocrystalline and coarse-crystalline Ag_2S powders, isolated Ag_2S nanoparticles, and different heteronanostructures with Ag_2S.

Usually, nanostructured Ag_2S synthesizes by hydrochemical deposition from aqueous solutions of $AgNO_3$ and Na_2S. Solutions of Na_3Cit or the disodium salt of EDTA (Trilon B) are used as complexing agents. Coarse-crystalline Ag_2S powder is prepared by hydrothermal synthesis from an aqueous reaction mixture of $AgNO_3$, Na_2S and Na_3Cit with subsequent heating of a matrix solution with the precipitated powder in a closed vessel at elevated temperature and pressure.

Hydrochemical deposition of Ag_2S nanopowders using of Trilon B, and also hydrothermal synthesis of Ag_2S powder, are described in study.[67]

Ag_2S deposition in the presence of Trilon B occurs according to the following reaction scheme:

$$2AgNO_3 + Na_2S \xrightarrow{EDTA-H_2Na_2} Ag_2S\downarrow + 2NaNO_3. \qquad (3)$$

Trilon B was added with constant stirring to $AgNO_3$ solution, and the prepared solution was then mixed with Na_2S solution. During mixing of the solutions, a sulfide formation reaction occurred instantaneously. All nanoparticles were deposited during 2 days. The average size D of Ag_2S nanoparticles in the deposited Ag_2S nanopowders was 58 ± 8 nm.

Disadvantages of the chemical deposition of Ag_2S from aqueous $AgNO_3$, Na_2S, and Trilon B solutions are the large size of prepared Ag_2S nanoparticles and the presence of a considerable amount of metallic Ag impurity.

Hydrochemical bath deposition using Na_3Cit is a well-known, simple and reliable universal "green" method which allows preparation of non-toxic colloidal solutions of Ag_2S nanoparticles, isolated Ag_2S nanoparticles and quantum dots with protective shells, Ag_2S/Ag heteronanostructures, nanocrystalline and coarse-crystalline powders of Ag_2S.[76,136–139] A weak aqueous solution of $AgNO_3$, which is widely applied in pharmacology and medicine and possesses antibacterial action, is usually used as a source of Ag^+ for Ag_2S synthesis. Conditions of hydrochemical bath deposition for preparing different forms of nanostructured Ag_2S, and the previously unknown possibilities of this method are generalized in study.[136]

Hydrochemical deposition of nanostructured Ag_2S with using Na_3Cit is an example of green chemistry because of the design of chemical products and processes that reduce or eliminate the use and generation of hazardous substances.[140] Indeed, hydrochemical bath deposition allows one to obtain valuable products from harmless substances using environmentally friendly methods.

In study,[136] different forms of nanostructured Ag_2S was synthesized by hydrochemical bath deposition from aqueous solutions of $AgNO_3$ and Na_2S used as sources of Ag^+ and S^{2-}.

Na_3Cit was used as a complexing agent and electrostatic stabilizer.

The solubility product (K_{sp}) of Ag_2S is very small (according to,[141] at 298 K, $K_{sp} = 6.3 \times 10^{-50}$), and Ag_2S is formed from an aqueous solution of $AgNO_3$ and Na_2S in a simple reaction

$$2AgNO_3 + Na_2S = Ag_2S\downarrow + 2NaNO_3, \tag{4}$$

where concentrations of S^{2-} and Ag^+ are related by $C_{S^{2-}} = C_{Ag^+}/2$. Small variation in the ratio of reagent concentrations as compared with the perfect reaction (4), introduction of a complexing agent, and control over synthetic conditions allow preparation of different forms of Ag_2S – from coarse-crystalline powder to colloidal nanoparticles.

A generalized scheme of synthesis of different types of nanostructured Ag_2S and Ag_2S/Ag heteronanostructures is shown in Fig. 7.

Coarse-crystalline Ag_2S powders are deposited almost instantly from an aqueous solution of $AgNO_3$ and Na_2S with a large excess concentration of S^{2-} ($C_{S^{2-}} \geq C_{Ag^+}$) both without and with addition of Na_3Cit as a complexing agent at room temperature in the dark (Fig. 7a). Synthesis with excess Na_2S and without addition of Na_3Cit led to the deposition of Ag_2S powder of particle size ~1000 nm. When Na_3Cit was added to reaction mixtures having excess Na_2S, the average size of Ag_2S particles decreased to ~200 nm.

If the concentration of S^{2-} is sufficient or differs slightly from the concentration required for the chemical bonding, all Ag^+ (*i.e.* $C_{S^{2-}} \approx C_{Ag^+}/2 + \delta$), then addition of Na_3Cit to the solution promotes the formation of Ag_2S nanoparticles and quantum dots (Fig. 7b). Deposition of Ag_2S takes place in neutral medium at pH ≈ 7 by the following reaction scheme

$$2AgNO_3 + (1 \pm \delta)Na_2S \xrightarrow{Na_3C_6H_5O_7} Ag_2S\downarrow + \ 2NaNO_3, \tag{5}$$

where $\delta \geq 0$. Some excess of Na_2S is necessary for synthesis of Ag_2S without an impurity of metallic Ag nanoparticles. Synthesis was carried out in a dark room.

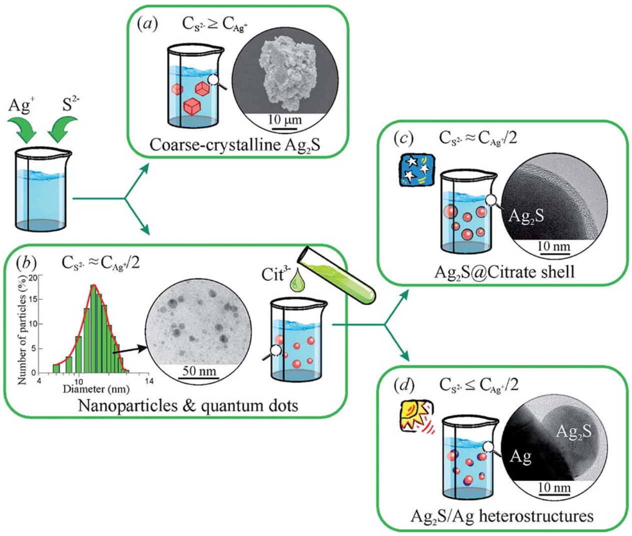

Fig. 7 Generalized scheme of the synthesis of various types of nanostructured Ag_2S and Ag_2S/Ag heteronanostructures: (a) coarse-crystalline Ag_2S; (b) Ag_2S quantum dots; (c) Ag_2S@C core–shell nanoparticle with carbon-containing citrate shell; (d) Ag_2S/Ag heteronanostructures. Reproduced from ref. 136 with permission from Wiley.

Na_3Cit has a triple role in aqueous solutions of $AgNO_3$ and Na_2S.

First, it is a complexing and stabilizing agent during deposition of Ag_2S nanoparticles, which occurs both in the light and dark (Fig. 7b). Second, during deposition in the dark, Na_3Cit is adsorbed on Ag_2S nanoparticles, impeding their agglomeration. In this case, an increased duration of deposition and use of reaction mixtures with an enhanced concentration of Na_3Cit leads to the formation of a protective citrate shell on the surface of Ag_2S nanoparticles (Fig. 7c). Third, during deposition in the light in aqueous solutions with lowered content of S^{2-}, Na_3Cit can reduce Ag^+ to metallic silver.[142]

During deposition in the light, Na_3Cit, as a reducing agent, takes part in a photochemical reaction

$$C_6H_5O_7{}^{3-} + 2Ag^+ \xrightarrow{h\nu} C_5H_4O_5{}^{2-} + CO_2 + H^+ + 2Ag\downarrow, \tag{6}$$

in which citrate ions ($C_6H_5O_7{}^{3-}$) reduce the Ag^+ present in the solution to metallic Ag nanoparticles and transform ($C_6H_5O_7{}^{3-}$) to acetone–1,3-dicarboxylate ions ($C_5H_4O_5{}^{2-}$). In this case, selection of the concentrations of $AgNO_3$, Na_2S, and Na_3Cit in the initial solution meeting the condition $C_{S^{2-}} \leq C_{Ag^+}/2$ makes it possible to deposit Ag nanoparticles along with Ag_2S nanoparticles and to synthesize Ag_2S/Ag heteronanostructures (Fig. 7d).

In principle, citric acid (harmless standardized food additive E330) can be used as a complexing agent for Ag^+, but its application in Ag_2S synthesis displaces the equilibrium into the acidic region, which is not desirable.

Nanosized Ag_2S powders were prepared from aqueous solutions of $AgNO_3$ and Na_2S containing Na_3Cit. The concentration of $AgNO_3$ was 50 mmol l^{-1}. The concentration of Na_2S in the initial reaction mixtures was slightly over half of the $AgNO_3$ concentration, *i.e.*, $C_{Na_2S} = (C_{AgNO_3}/2) + \delta$ with $\delta = 0.5$ mmol l^{-1}.[136] The average particle size (D) in the examined Ag_2S nanopowders was about 46 ± 7 nm.

The technology for the production of Ag_2S nanopowders with preset nanoparticle size from 20 to 500 nm by hydrochemical deposition has been patented.[143]

Stable colloidal solutions of Ag_2S quantum dots were prepared from the reaction mixtures with $AgNO_3$ concentrations (C_{AgNO_3}) from 0.3125 to 2.5 mmol l^{-1}. The Na_2S concentration (C_{Na_2S}) in the reaction mixtures was slightly over half of the $AgNO_3$ concentration (*i.e.*, $C_{Na_2S} = (C_{AgNO_3}/2) + \delta$, where $\delta = 0.01$ mmol l^{-1}).[136]

According to the dynamic light scattering (DLS) data, the size of Ag_2S quantum dots in colloidal solutions was ≤20 nm. The DLS zeta-potential measurements of colloidal solutions confirmed that these solutions remained stable for >100 days. The particle size distributions for the colloidal solutions with different size of Ag_2S quantum dots and the appearance of these colloidal solutions are shown in Fig. 8a and b.

The zeta potential (ζ) of quantum dots in a solution is an indicator of the system stability. The DLS measurements revealed that 3 days after synthesis, the ζ was −45 to −28 mV, and the quantum dot size was 2–13 nm. The ζ and size of Ag_2S quantum dots measured 100 days after synthesis of colloidal solutions remained almost unchanged.[136] The comparison of the ζ with the average size (D_{DLS}) of quantum dots for synthesized colloidal solutions 100 days after synthesis is displayed in Fig. 8c. The D_{DLS} of quantum dots was 2 to 17 nm, the value of ζ varied from −49 to −29 mV, and the average ζ was -35 ± 10 mV. It can be seen that, the smaller is the absolute value of ζ, the larger is the size of Ag_2S quantum dots.

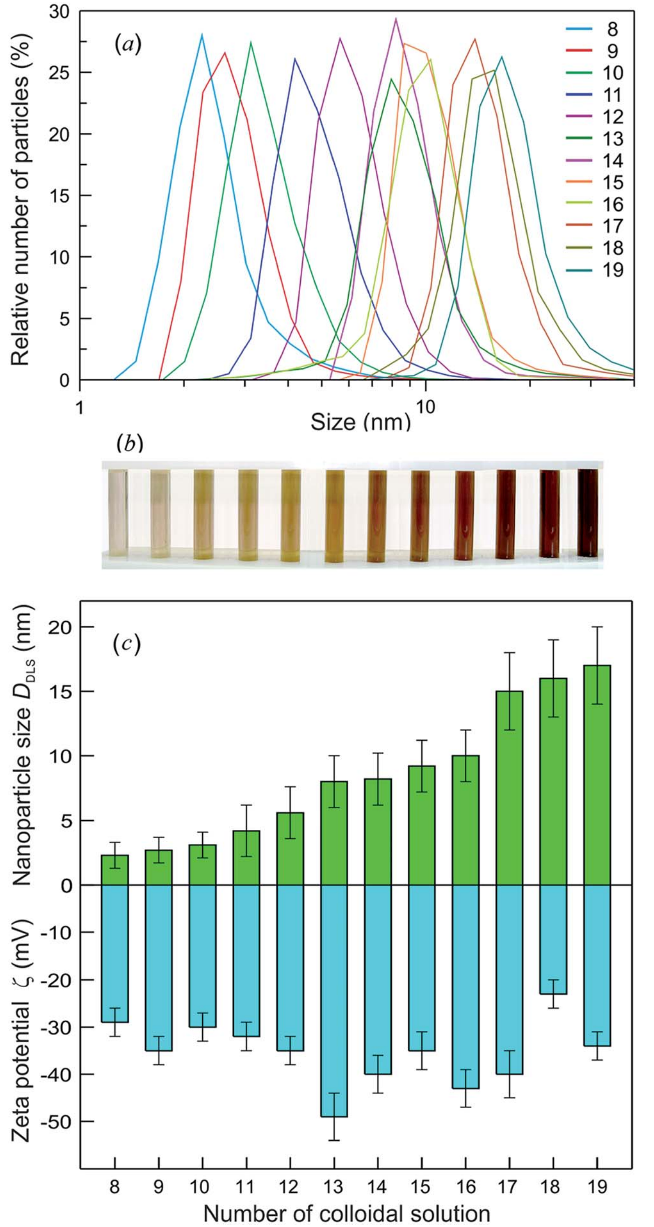

Fig. 8 (a) The particle size distributions measured by DLS for colloidal solutions with different average sizes of Ag_2S QDs from 2.3 to 17.0 nm, (b) the appearance of these colloidal solutions, and (c) the average size D_{DLS} and zeta potential ζ of Ag_2S QDs in colloidal solutions measured 100 days after synthesis.

Fig. 9 presents the size-dependent PL emission spectra of Ag_2S colloidal solutions in which the fluorescence of Ag_2S quantum dots is tunable from ~1176 to ~960 nm by decreasing the nanoparticle D_{DLS} from 15.0 to 2.3 nm. According to,[56] the PL peak for Ag_2S quantum dots with a size about 1.5 nm was observed at ~640 nm (see Fig. 9). The PL emission peaks shifted from ~960 to ~1170 nm with the size of Ag_2S quantum dots increasing from ~2.3 to 4.2 nm and remained constant at 1166–1176 nm with an increase of the quantum dot size from ~4.2 to >15 nm. The continuous blue shift of the PL emission of Ag_2S quantum dots from ~1176 to ~640 nm can be attributed to the strengthened quantum confinement effect and increase in band gap E_g which resulted from the decreasing size of Ag_2S quantum dots. This hypothesis is in agreement with experimental data[144] on the size-dependent band gap of Ag_2S nanopowders. An almost constant position of the PL emission peaks at ~1166 to 1176 nm for the Ag_2S quantum dots with a boundary value of ≥4.2 nm is evidence for transition from the strong quantum confinement regime to a weak quantum confinement regime. According to this hypothesis, the estimated Ag_2S exciton radius (R_{exc}) is less than half of boundary size of 4.2 nm (*i.e.*, ≤2.1 nm).

The R_{exc} for Ag_2S, which is calculated by formula (1), is about 1.4 ± 0.1 nm, and the exciton diameter is about 3 nm. According to an analogous estimation,[145] the Ag_2S exciton diameter ranges from 3.0 to 4.4 nm. A strong blue shift for a quantum dot of size 1.5 nm agrees with data[145] on the Ag_2S exciton diameter. An estimated exciton diameter ~3 nm for Ag_2S is in satisfactory agreement with the experimental result (4.2 nm),[136] which follows from the size-dependent PL emission spectra (see Fig. 9).

The technology for preparing aqueous colloidal solutions of stable Ag_2S quantum dots has been patented.[146]

$Ag_2S@C$ nanoparticles with a carbon-containing citrate shell were found in colloidal solutions prepared from an aqueous solutions of $AgNO_3$ and Na_2S at concentrations of 5.0 and

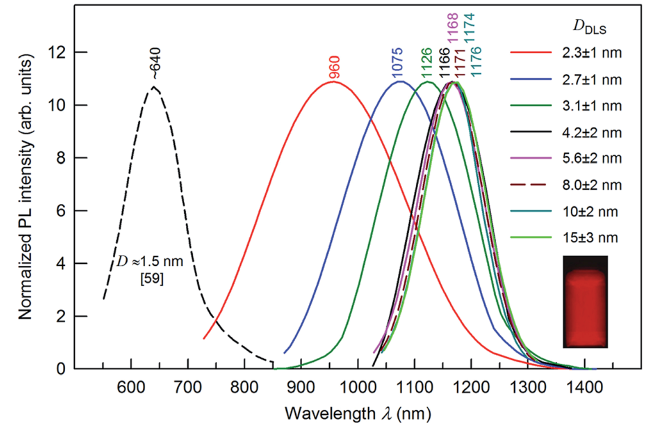

Fig. 9 The size-dependent PL emission spectra of Ag_2S colloidal solutions with quantum dot size D_{DLS} from 2.3 to 15.0 nm under an excitation of 658 nm. For comparison, the dashed line shows the position of the PL emission peak for Ag_2S quantum dots of size ~1.5 nm.[56] The wavelengths corresponding to the maxima of the PL peaks are indicated. The inset presents a fluorescence image of Ag_2S colloidal solution of quantum dot size ~8 nm.

2.5 mmol l^{-1} or 50 and 25 mmol l^{-1}, respectively; the Na_3Cit concentration varied from 5 to 100 mmol l^{-1}.[68,136,147] Synthesis was carried out at room temperature in the dark.

The X-ray diffraction (XRD) patterns of Ag_2S nanopowders deposited from a reaction mixture of $AgNO_3$, Na_2S and Na_3Cit with concentrations of 5.0, 2.5 and 5.0 mmol l^{-1}, respectively, are shown in Fig. 10A. These nanopowders can be distinguished by their dwell time in the solution (from 20 to 1200 min). The quantitative analysis of the XRD patterns and comparison with data[148] have shown that the observed set of diffraction reflections corresponds to nonstoichiometric monoclinic (space group $P2_1/c$) acanthite $\sim Ag_{1.93}S$. The amorphous carbon-containing shell is not visible on the XRD patterns.

The Ag_2S nanoparticles extracted from the colloidal solutions have an amorphous shell (Fig. 10B). Other things being equal, the thickness of the shell grows when the nanoparticle dwell time in the colloidal solution containing $C_6H_5O_7{}^{3-}$ (Fig. 10B(a)–(d)) increases, and when the concentration of Na_3Cit in the solution increases. A filtered image of area 1 isolated by a white square is shown in Fig. 10B(a). The determination of the interplanar distances of cores confirmed a monoclinic structure of the colloidal Ag_2S nanoparticles. Fig. 10C(e) shows as an example of the XRD pattern of the core of the nanoparticle presented in Fig. 10B(a). The observed set of spots (−1−11), (−111), (020), and (−212) corresponds to the [101] plane of the reciprocal lattice of the monoclinic (space group $P2_1/c$) α-Ag_2S phase with an acanthite structure.

According to the energy-dispersive X-ray spectroscopy (EDX) results, the content of Ag and S in the colloidal core–shell nanoparticles corresponds to $Ag_{1.95-1.98}S$ (Fig. 10C(f)–(h)). The content of carbon is proportional to the intensity of the C Kα line and increases with growth of the shell thickness (Fig. 10C(f)–(h)). Hence, the shell of sulfide nanoparticles contains carbon and is a citrate shell.

Indeed, the three carboxylate groups of Na_3Cit have strong affinity for Ag^+, which favors the attachment of citrate groups on the surface of the Ag_2S nanoparticles and prevents them from aggregating into large particles. In other words, $C_6H_5O_7{}^{3-}$ are adsorbed on the surface of nanoparticles and form a citrate carbon-containing shell that prevents the growth and agglomeration of the nanoparticles.

In the solutions with Na_3Cit, the $C_6H_5O_7{}^{3-}$ are adsorbed on the surface of Ag_2S nanoparticles and first form an uneven, discontinuous shell. As the Ag_2S nanoparticle dwell time in the solution increases, the discontinuities are gradually filled with citrate complexes, and a continuous carbon-containing shell is formed. Gradual adsorption of the citrate complexes by the formed coating promotes smoothing of the shell surface and the growth of the shell thickness.[68,136] A continuous shell is formed when $C_{S^{2-}} = C_{Ag^+}/2$ and $C_{Ag^+}/4 \le C_{Cit^{3-}} \le C_{Ag^+}$.

The presence of a protective citrate shell is important for the PL of Ag_2S nanoparticles. A decrease in nanoparticle size should be accompanied by a blue shift of the PL peak. However, the observed shift may be less than expected because of the formation of surface trap states in the band gap and electron–phonon coupling. To induce a blue shift, one should suppress the formation of surface trap states in the band gap of Ag_2S nanoparticles. If the core size is constant, a growth of the protective

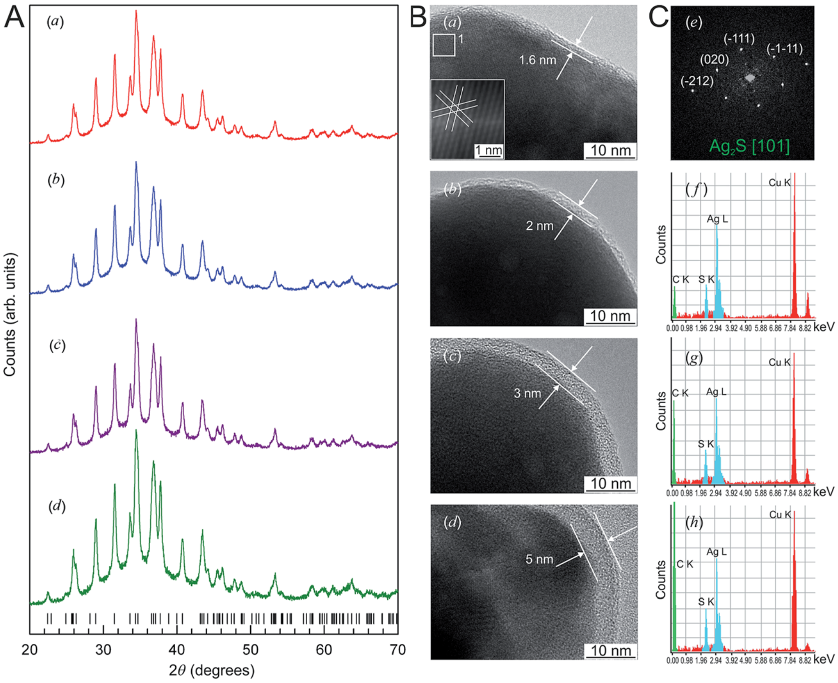

Fig. 10 (A) The XRD patterns of monoclinic (space group $P2_1/c$) Ag_2S nanoparticles and (B) HRTEM images of silver sulfide nanoparticles and the growth of the carbon-containing citrate shell thickness as a function of the nanoparticle dwell time in the solution: (a) 20 min, (b) 40 min, (c) 420 min, (d) 1200 min. Vertical marks on XRD patterns indicate the positions of diffraction reflections of the nonstoichiometric monoclinic α-$Ag_{1.93}S$ phase. (C) (e) Selected area of electron diffraction (SAED obtained from the area 1 of HRTEM nanoparticle (a); (f), (g), and (h) cumulative elemental EDX patterns of nanoparticles (b), (c), and (d), respectively). Reproduced from ref. 136 with permission from Wiley.

carbon-containing citrate shell thickness leads to weak intensity enhancement of the PL peaks and a small shift of peaks into the region of lower wavelength (Fig. 11). The position of PL peaks does not depend on the size of an Ag_2S core of ≥12 nm.

According to,[68,136,147] hydrochemical bath deposition allows preparation of Ag_2S@C core–shell nanoparticles with pre-assigned sizes of the Ag_2S core from 10 and 50 nm and pre-assigned carbon-containing citrate shell thickness from 1.5 to 10 nm.

The process of manufacture of Ag_2S@C core–shell nanoparticles with a protective citrate carbon-containing shell by hydrochemical deposition has been patented.[149]

Comparison of advantages and disadvantages of the main methods for synthesis of different forms of nanostructured Ag_2S is presented in summary Table 1.

From a comparison of different methods for the synthesis of nanostructured Ag_2S, it follows that the most universal method is hydrochemical deposition. This method allows synthesis of colloidal solutions of Ag_2S nanoparticles, isolated Ag_2S nanoparticles and quantum dots with protective shells, Ag_2S/Ag heteronanostructures, nanocrystalline and coarse-crystalline powders of Ag_2S. All the forms of nanostructured Ag_2S with controllable size can be prepared from the same chemical reagents by varying only their concentrations in solution and the conditions of synthesis. The important advantage of hydrochemical deposition in comparison with other methods is the reproducibility of obtained results.

Hydrothermal and solvothermal synthetic methods are most promising for the preparation of Ag_2S in the form of sufficiently large objects with different morphologies (*e.g.*, leaf-like nanosheets, flake or star-shaped crystallites, faceted crystals, tetrahedral and hexagonal particles, hollow particles, *etc.*). Such objects can have the size from hundreds of nanometers to tens of micrometers.

The preferred method for preparation of Ag_2S nanowires with a high aspect ratio (length/diameter) is template synthesis using silver foil or an aluminum oxide template.

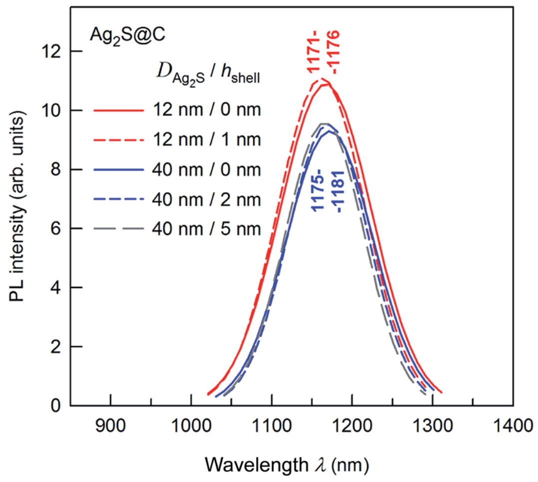

Fig. 11 Effect of citrate shell thickness on the PL emission spectra of Ag_2S@C core–shell nanoparticles. The wavelengths corresponding to the maxima of the PL peaks are indicated. The wavelength of excitation is 658 nm.

3. Crystal structure of Ag_2S phases

Ag_2S has three basic polymorphic modifications: monoclinic α-Ag_2S acanthite, cubic β-Ag_2S argentite, and high-temperature cubic γ-Ag_2S sulfide. Structures of the different phases of Ag_2S were defined originally in studies[150–152] and specified later in works.[153–155] In works,[150–153] the structure of different Ag_2S phases was determined on samples of natural minerals such as acanthite and also pseudomorphic acanthite that preserved the cubic morphology of argentite. In works,[154,155] an artificial crystal or a powder of Ag_2S were used for structure determination. In all cases, these were coarse-grained samples with grain (particle) size of 5–10 μm or larger.

Crystal structures of these phases are fairly complex. Hence, in most experimental works devoted to synthesis and properties of Ag_2S, description of the crystal structure of the synthesized sulfide is lacking[57,156,157] or it is made by comparing experimental XRD or TEM results[46,49,56,57,70,73,100,117,158–160] with old XRD data.[150] So, in studies,[46,49,159–161] without performing full-profile structure refinement, it was suggested that Ag_2S synthesized in the form of a film, nanocrystalline powder or nanoparticles has a crystal structure of natural acanthite, whereas in work[75] it was assumed that synthesized Ag_2S film had the structure of argentite. However, the crystal structure of synthetic Ag_2S may have considerable differences that affect the properties of Ag_2S. For example, with regard to the XRD patterns of Ag_2S nanoparticles, authors[159] found a set of spots corresponding to the monoclinic α-Ag_2S phase with an acanthite structure, as well as several spots that could not be identified in a monoclinic acanthite-type structure. According to,[159] the atomic ratio of Ag to S was estimated to be 1.7 and even 1.1 for nanoparticles with a size of ∼10 and ∼6 nm, respectively. In other words, the examined nanoparticles had the nonstoichiometric chemical composition $Ag_{1.7}S$ and even $Ag_{1.1}S$.

Careful determination of crystal structures of coarse-crystalline and nanocrystalline acanthite α-Ag_2S and argentite β-Ag_2S has been performed recently in studies.[118,148,162–166]

3.1 Artificial coarse-crystalline α-Ag_2S

According to,[150,153] the structure of acanthite α-Ag_2S can be interpreted as a result of distortion of the β-Ag_2S argentite structure. Indeed, the unit cells of α-Ag_2S acanthite proposed in studies[150,153] have axes that can be represented as a combination of axes a_{bcc}, b_{bcc} and c_{bcc} of the unit cell of bcc argentite.

Recently,[118,163] the crystal structure of α-Ag_2S acanthite was refined for the first time on synthesized artificial samples of coarse-crystalline powder of Ag_2S with the use of full-profile analyses of XRD data. The average particle size D of coarse-crystalline Ag_2S powder was estimated from the value of specific surface area $S_{sp} = 1.6 \pm 0.1$ m^2 g^{-1} and was ∼515 nm.

According to EDX results, the content of Ag and S in the synthesized coarse-crystalline Ag_2S powder was 86.8 ± 0.4 and 12.9 ± 0.1 wt%, which corresponds to stoichiometric Ag_2S.

The refinement of the crystal structure of synthesized Ag_2S provided the following results: synthesized Ag_2S had a crystal structure of α-Ag_2S acanthite type; monoclinic (space group

Table 1 Methods of synthesis of different forms of nanostructured Ag_2S

Method	Main reagents[a]	Forms of nanostructured Ag_2S	Advantages	Disadvantages	Ref.
Hydro-thermal method	$AgNO_3$, CS_2, Na_2S, NH_4OH, $(NH_2)_2CS$, $C_{19}H_{42}BrN$, $N_2S_2O_3$, Ag $[S_2P(OR)_2]$ (R = C_nH_{2n+1}), $CH_3(CH_2)_{11}SH$, PVP	Leaf-like nanosheets, faceted and cubic nanocrystals, hollow nanohexagons, tetrahedral and rice-shaped nanoparticles	Large scale of products	Complicated process, elaborate equipment, non-uniform size distribution, toxic reagents	108, 110, 111, 113, 114 and 117
Solvo-thermal method	$AgNO_3$, CS_2, NH_4OH, C_2H_5OH, PVP	Flake or star-shape nanocrystallite	Low cost reagents	Elaborate equipment, large and non-uniform size, toxic reagents	107
Solvo-thermal method	$AgNO_3$, $C_{13}H_{11}NS$, $C_{19}H_{42}BrN$, C_4H_9OH	Spherical nanoparticles	Good re-producibility	Elaborate equipment, non-uniform size	132
Solvo-thermal method	$C_{18}H_{31}AgO_2$, $C_{18}H_{32}O_2$, C_2H_5OH	Monodisperse nanocrystals	Small size, uniform size distribution	Elaborate equipment	133
Hydro-chemical deposition	$AgNO_3$, NH_4OH, $Na_2S_2O_3$, $(NH_2)_2CS$	Rod-like nanocrystals, nanowires, worm-like nanoparticles, nano-polyhedrons	Easy operation, high yield, good re-producibility	Non-uniform size distribution	106 and 109
Template method	$AgNO_3$, $C_4H_6O_2$, $(NH_4)_2S_2O_6(O_2)$, *n*-heptane, $Na_2S_2O_3$, $C_{19}H_{42}BrN$, CS_2	Microsphere with surface flower-like structure, hollow nanospheres	Controllable size and morphology	Complicated sequential process	112 and 115
Thermal decomposition (hot-injection process)	C_7H_5AgOS, $C_{24}H_{51}P$, $(C_2H_5)_2NCSSAg$, silver xanthate	Cube-shaped and spherical nanocrystals	Controllable size and morphology, simplicity, safety	Elaborate equipment, sequential process	39, 102–104
Pyrolysis	$AgNO_3$, S, $C_{18}H_{35}NH_2$	Nanoparticles	Uniform size	Low yield	131
Thermal decomposition	$(C_2H_5)_2NCS_2Ag$, $CH_3(CH_2)_{11}SH$	Quantum dots	Controllable small size, narrow size distribution	Complicated sequential process	134
Hydro-thermal method	$AgNO_3$, Na_2S, $C_3H_6O_2S$, CH_3COOH, NaOH	Quantum dots	Controllable small size, narrow size distribution	Sequential process	135
Gas–solid reaction method on Ag substrate	Ag foil, H_2S/O_2 gas mixture	Nanowires	High aspect ratio, mono-crystallinity	Elaborate equipment, complicated process	121
Solvo-thermal method	$AgNO_3$, $CH_3(CH_2)_{17}NH_2$	Ultralong nanowires	High aspect ratio, mono-crystallinity	Elaborate equipment	120
Template solvo-thermal method with cation exchange	S, $Cd(CH_3COO)_2$, CuCl, $AgNO_3$, anhydrous C_2H_5OH, $(CH_2OH)_2$, $NH_2CH_2CH_2NH_2$	Nanowires	Controllable phase composition	Elaborate equipment, complicated sequential process	124 and 125
Hydro-chemical deposition	$AgNO_3$, Na_2S, Na_3Cit or Trilon B	Nanoparticles, quantum dots	Large scale of products, controllable size, safety, simplicity, non-toxic reagents	Possible presence of metallic Ag impurity in Ag_2S	67, 68, 136 and 144

[a] PVP – polyvinylpyrrolidone $(C_6H_9NO)_n$.

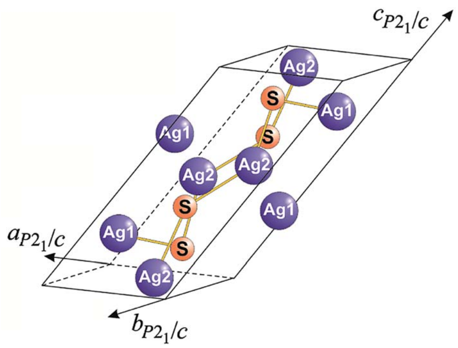

Fig. 12 Monoclinic (space group $P2_1/c$) unit cell of Ag_2S with an acanthite structure (only the atoms entering into the unit cell and the nearest bonds between them, Ag1–S and Ag2–S, of length 0.2511 and 0.2548 nm, respectively, are shown). Reprinted from ref. 118 with permission from Elsevier.

$P2_1/c$) unit cell parameters were $a = 0.42264(2)$ nm, $b = 0.69282(3)$ nm, $c = 0.95317(3)$ nm and $\beta = 125.554(2)^\circ$; the site occupancy factor of all crystallographic positions by Ag and S atoms was 1.0; the Rietveld reliability factor R_I (R_B) was 0.0247. These unit cell parameters were in good agreement with the data.[153]

Thus, artificial coarse-grained Ag_2S is stoichiometric. The arrangement of Ag and S atoms in the unit cell of artificial monoclinic (space group $P2_1/c$) Ag_2S with an α-Ag_2S acanthite type structure is displayed in Fig. 12.

3.2 Crystal structure and nonstoichiometry of nanostructured α-Ag_2S

Determination of the influence of nanoparticle size on their nonstoichiometry is a fundamental scientific problem.

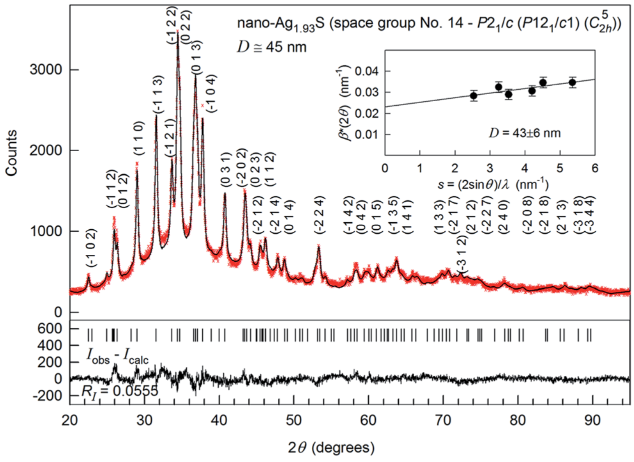

Fig. 13 The experimental (×) and calculated (——) XRD patterns of $Ag_{1.93}S$ nanopowder deposited from a reaction mixture of $AgNO_3$, Na_2S and Na_3Cit having concentrations 0.05, 0.025, and 0.025 mol l^{-1}, respectively. The difference between the experimental and calculated XRD patterns ($I_{obs} - I_{calc}$) is shown in the lower part of the figure. The inset presents the estimate of the average CSRs size from the broadening of non-overlapping diffraction reflections. The XRD pattern is recorded in CuKα_1 radiation. Reproduced from ref. 148 with permission from the PCCP Owner Societies.

A nanostructured Ag_2S has been studied extensively in the past two decades. However, until lately, there were no experimental works on the determination of the crystal structure of nanocrystalline Ag_2S.

Determination of the structure of nanocrystalline Ag_2S has been done in study.[148]

The nanocrystalline powder of Ag_2S was synthesized by chemical deposition from aqueous solution of $AgNO_3$ and Na_2S containing Na_3Cit as a complexing and stabilizing agent.

The XRD pattern of synthesized Ag_2S nanopowder is shown in Fig. 13. According to the BET data, the particle size of the nanopowder was 44 ± 5 nm.

Preliminary analysis revealed that the synthesized nanocrystalline powder had a monoclinic (space group $P2_1/c$) α-Ag_2S acanthite-type structure. The XRD reflections of the nanopowder were broadened and, therefore, the reflections located close to each other overlapped. The average size D of coherent scattering region (CSR) estimated from broadening of non-overlapping diffraction reflections (−102), (110), (−113), (−104), (031) and (014) was 43 ± 6 nm.

The coordinates of Ag and S atoms and unit cell parameters for Ag_2S nanopowder (Table 2) are close to those for coarse-crystalline Ag_2S. However, the occupancy of crystallographic positions 4(e) by Ag1 and Ag2 atoms was ~0.97 and ~0.96, respectively (Table 2). Hence, Ag_2S nanoparticles of size less than ~50 nm are nonstoichiometric, have a composition of $\sim Ag_{1.93}S$ and contain vacant sites in the metal sublattice.

3.3 Acanthite α-Ag_2S–argentite β-Ag_2S phase transformation

For the first time, complex *in situ* high-temperature XRD and SEM study of the α-Ag_2S (acanthite) to β-Ag_2S (argentite) phase transformation in nanocrystalline and coarse-crystalline powders of Ag_2S has been carried out in works.[162,165,166] Until lately, few data on acanthite–argentite phase transformation were obtained only on bulk coarse-crystalline Ag_2S samples.

The low-temperature monoclinic phase α-Ag_2S (acanthite) exists at temperatures below ~450 K. Argentite β-Ag_2S has a bcc sublattice of S atoms and exists in the temperature interval 452–859 K.

When argentite β-Ag_2S is cooled below 450 K under equilibrium conditions, a polymorphous phase transformation takes place that gives rise to monoclinic acanthite α-Ag_2S. This transformation is accompanied by distortion of the bcc sublattice of S atoms to the monoclinic sublattice. The Ag atoms statistically distributed in positions of the bcc structure of argentite are concentrated in the positions of the monoclinic structure of acanthite, and occupy them with probability close to 1.

To precisely determine the phase transformation temperature, Ag_2S powders were studied *via* differential thermal analysis-differential thermal gravimetry (DTA-DTG) upon heating and cooling. During heating, the DTA curves had one endothermic peak at about 449–450 K, which corresponded to the α-Ag_2S (acanthite)–β-Ag_2S (argentite) phase transformation. In cooling from 500 K to room temperature, the DTA dependencies exhibited an exothermal peak related to the argentite-

Table 2 Refined crystal structure of monoclinic (space group no. 14 – $P2_1/c$ ($P12_1/c1$)) $Ag_{1.93}S$ nanopowder with an α-Ag_2S acanthite-type structure and particle size ~45 nm:[148] $Z = 4$, $a = 0.4234(3)$ nm, $b = 0.6949(3)$ nm, $c = 0.9549(5)$ nm, and $\beta = 125.43(6)°$

Atom	Position and multiplicity	Atomic coordinates x/a	y/b	z/c	Occupancy	$B_{iso} \times 10^{-4}$ (pm^2)
Ag1	4(e)	0.0715	0.0151(0)	0.3093(9)	0.97	10.05(5)
Ag2	4(e)	0.7264	0.3240(9)	0.4375(0)	0.96	7.44(6)
S	4(e)	0.4920	0.2339(8)	0.1321(1)	1.00	1.960

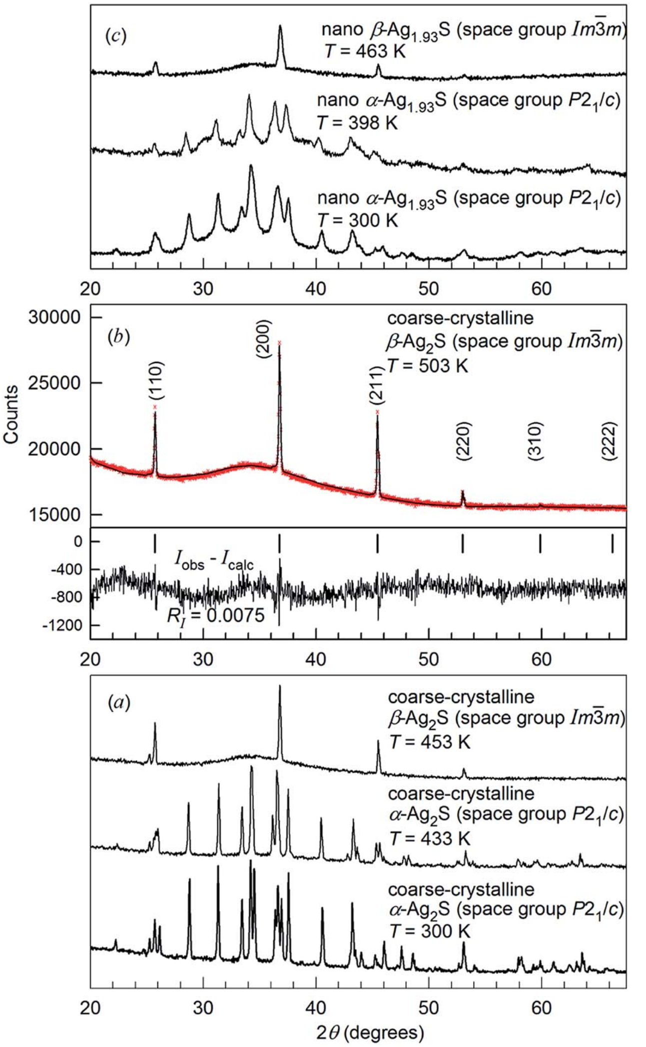

Fig. 14 Evolution of XRD patterns of silver sulfide at heating.[162,165,166] (a) XRD pattern of coarse-crystalline silver sulfide with a monoclinic (space group $P2_1/c$) α-Ag_2S acanthite-type structure at 300 and 433 K, and with a cubic (space group $Im\bar{3}m$) β-Ag_2S argentite-type structure at 453 K. (b) Experimental (×) and calculated (——) XRD patterns of coarse-crystalline silver sulfide with cubic (space group $Im\bar{3}m$) β-Ag_2S argentite-type structure at 503 K and the difference ($I_{obs} - I_{calc}$) between the experimental and calculated XRD patterns; the ticks correspond to reflections of cubic argentite β-Ag_2S. (c) XRD patterns of nanocrystalline $Ag_{1.93}S$ with a monoclinic (space group $P2_1/c$) acanthite-type structure at 300 and 398 K, and with a cubic (space group $Im\bar{3}m$) β-Ag_2S argentite-type structure at 463 K, respectively. Reproduced from ref. 162 and 166 with permission from the PCCP Owner Societies.

to-acanthite phase transformation towards a lower temperature range by ~20 K. The presence of the temperature hysteresis (T_{trans}) means this was a first-order reversible acanthite–argentite transformation. The enthalpy of the phase transformation (ΔH_{trans}) was ~3.7–3.9 kJ mol^{-1}, which is very close to that determined in works[167–170] ($\Delta H_{trans} = 4.0 \pm 0.5$ kJ mol^{-1}).

The XRD patterns for coarse-crystalline Ag_2S powder collected at 300, 433, 453 and 503 K, and the XRD patterns for nanocrystalline Ag_2S powder at 300, 398 and 463 K are shown in Fig. 14. The XRD patterns recorded at $T < 450$ K (Fig. 14a and c) contained the diffraction reflections of monoclinic (space group $P2_1/c$) α-Ag_2S acanthite. The average particle size D in the nanopowder estimated from broadening of diffraction reflections was ~60 nm. According to the DTA data, the transformation of acanthite α-Ag_2S into argentite β-Ag_2S takes place at ~449–450 K. Indeed, the XRD patterns recorded at $T \geq 453$ K contained diffraction reflections of cubic (space group $Im\bar{3}m$) β-Ag_2S argentite. The refinement of the XRD pattern (Fig. 14b) showed that coarse-crystalline Ag_2S at 503 K contained one phase with a cubic (space group no. 229 – $Im\bar{3}m$ ($I4/m\bar{3}2/m$) (O_h^9)) structure of β-Ag_2S argentite (Table 3). According to high-temperature XRD data,[162,166] the unit cell of β-Ag_2S argentite includes two Ag_2S formula units. Two S atoms occupy crystallographic positions 2(a) and form a bcc sublattice. Four Ag atoms in β-Ag_2S argentite are statistically distributed in 54 positions 6(b) and 48(j) with the occupation probabilities ~0.0978 and ~0.0711, respectively (Table 3).

A structure with such small occupancies can be stable only if the mobility of Ag atoms/ions is very high. The amount of Ag^+ in argentite β-Ag_2S is much smaller than the number of sites of the cation sublattice. Therefore, significant positional disorder in an arrangement of Ag^+ and a gigantic (>92%) concentration of vacant sites facilitate the "jumping" of cations and provide the superionic conductivity of the β-Ag_2S phase.

The unit cell of cubic (space group $Im\bar{3}m$) β-Ag_2S argentite is shown in Fig. 15. Detailed crystallographic information on β-Ag_2S argentite presented as "Crystal structure data" in the CIF-file attached to article.[162] This CIF number 1062400, which was placed on the Cambridge Crystallographic Data Centre (CCDC) website, can be found at the following electronic address.[171]

Thus, heating of monoclinic α-Ag_2S acanthite up to ~449–450 K leads to a polymorphic phase transition with the formation of bcc β-Ag_2S argentite.

SEM images of the acanthite-to-argentite transformation occurring in nanocrystalline and coarse-crystalline Ag_2S powders are shown in Fig. 16.

Table 3 Refined crystal structure of cubic (space group no. 229 – $Im\bar{3}m$ ($I4/m\bar{3}2/m$) (O_h^9)) coarse-crystalline silver sulfide β-Ag_2S (β-$Ag_{2.01}S$) with an argentite-type structure at 503 K:[162,166,166] $Z = 2$, $a = b = c = 0.4874(1)$ nm

Atom	Position and multiplicity	Atomic coordinates x	y	z	Occupancy	$B_{iso} \times 10^{-4}$ (pm^2)
Ag1	6(b)	0	0.5	0.5	0.0978(7)	0.50
Ag2	48(j)	0	0.3306(5)	0.4122(7)	0.0711(0)	0.50
S	2(a)	0	0	0	1.00(0)	0.50

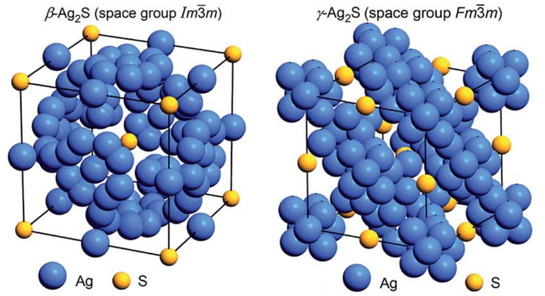

Fig. 15 The arrangement of Ag and S atoms in the unit cells of cubic (space group $Im\bar{3}m$) β-Ag_2S argentite[162] and cubic (space group $Fm\bar{3}m$) γ-Ag_2S.[155] Positions of silver sublattices on which Ag atoms are statistically distributed are shown. Reproduced from ref. 162 with permission from the PCCP Owner Societies.

In the upper row (Fig. 16a–c) the initial nanopowder with a surface area (for which the elemental chemical composition was determined by EDX) as well as the cumulative elemental EDX pattern of the initial powder are shown. According to the EDX data (Fig. 16c), the content of Ag and S in the Ag_2S nanopowder determined from the integral intensities AgL and SK lines were 86.8 ± 0.4 and 13.1 ± 0.1 wt%. This corresponds to a sulfide which is close to the stoichiometric composition of Ag_2S but with small deficiency of silver. The second row (Fig. 16d–f) show a SEM image of the electron beam-heated surface area, upon which argentite particles are growing, and of the same area (side view) with grown argentite crystals.

Short pyramidal nuclei of argentite crystallites (whose base was about 50–80 nm in thickness) appeared on the surface of Ag_2S powder particles ~30 s after the start of heating. As a result of heating, the nuclei grew quickly, taking the shape of whiskers, and in ~5 min covered the entire surface of the acanthite particle.

The sequence of formation and growth of argentite nanoparticles can be conventionally divided into four stages. First, as a result of electron-beam irradiation of acanthite, the particles are heated. Second, the phase transformation leads to the formation of argentite, so the appearance and growth of argentite nuclei take place on the surface of acanthite particles. The third stage is connected with the growth of argentite particles as a result of further heating and the argentite nuclei interacting with the low-temperature phase of acanthite acting as a donor. The growth of argentite particles ends at the fourth stage when no low-temperature acanthite remains in the surface layer.

The formation of argentite was also confirmed by HRTEM data. Fig. 17 demonstrates the HRTEM and TEM images of Ag_2S nanopowder before and after radiation heating.[162] In Fig. 17a, the interplanar distance is 0.309 nm and clearly visible, which

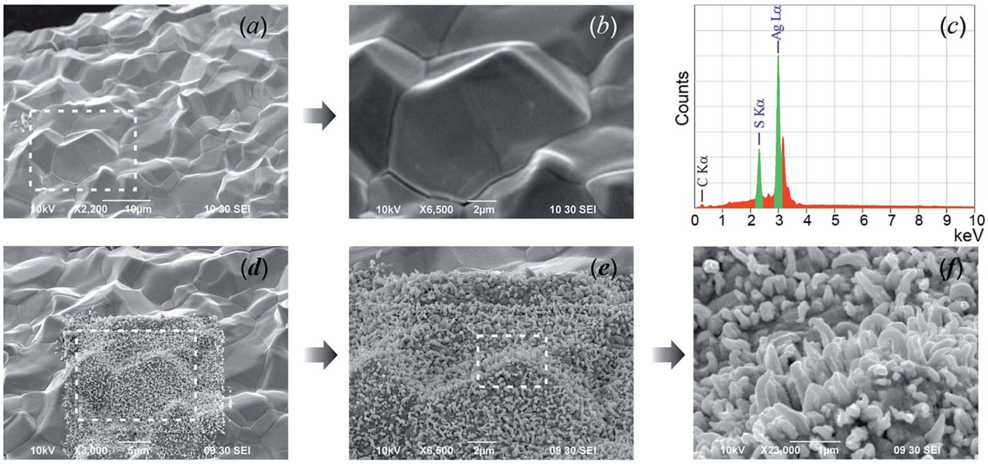

Fig. 16 The transformation of acanthite α-Ag_2S into argentite β-Ag_2S. Upper row: (a and b) the initial nanopowder and (c) its cumulative elemental EDX pattern. Second row: (d–f) the argentite particles are growing on the electron beam-heated surface area. The white dotted lines show the surface areas of Ag_2S powders heated by the electron beam. Reproduced from ref. 162 with permission from the PCCP Owner Societies.

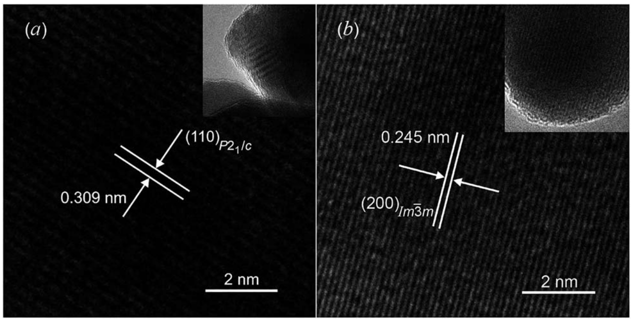

Fig. 17 HRTEM images of silver sulfide nanoparticles: (a) the interplanar distance (0.309 nm) observed before heating corresponds to monoclinic silver sulfide with an α-Ag_2S acanthite-type structure; (b) the interplanar distance (0.245 nm) observed after heating corresponds to a cubic silver sulfide with β-Ag_2S argentite-type structure. The insets show the TEM images of nanoparticles at lower magnification. Reproduced from ref. 162 with permission from the PCCP Owner Societies.

coincides with the distance $d_{(110)}$ between atomic planes (110) of Ag_2S with a monoclinic (space group $P2_1/c$) α-Ag_2S acanthite structure. Upon radiation heating of the nanopowder, the HRTEM image exhibits an interplanar distance of 0.245 nm (Fig. 17b). This corresponds to the distance between the atomic planes (200) of cubic (space group $Im\bar{3}m$) Ag_2S with a β-Ag_2S argentite structure. The insets in Fig. 17 correspond to the TEM images of these nanopowders of Ag_2S before and after heating.

3.4 Crystal structure of the γ-Ag_2S phase and distributions of Ag atoms in cubic Ag_2S

At temperatures above 860 K, Ag_2S contains a cubic (space group $Fm\bar{3}m$ ($F4/m\bar{3}2/m$) (O_h^5)) γ-Ag_2S phase. The unit cell of the γ-Ag_2S phase includes four formula units of Ag_2S ($z = 4$). The first structural model of high-temperature cubic γ-Ag_2S was proposed in study.[172] According to,[172] four S atoms occupy crystallographic positions 4(a) and form a fcc sublattice, and eight Ag atoms are statistically distributed in 8(c) and 32(f) positions. Blanton *et al.*,[155] using high-temperature XRD data, refined the model[172] by distributing Ag atoms on positions 48(i) also (Table 4). According to,[155] at 923 K, eight Ag atoms are statistically distributed in 88 positions 8(c), 32(f) and 48(i) with the occupation probabilities ~0.088, ~0.15, and ~0.027, respectively. Model[155] suggests some Ag deficiency in the γ-phase corresponding to nonstoichiometric $Ag_{1.7}S$. Fig. 15 shows the crystal structure of γ-Ag_2S proposed in study.[155]

Table 4 Crystal structure of cubic (space group no. 225 – $Fm\bar{3}m$ ($F4/m\bar{3}2/m$) (O_h^5)) γ-Ag_2S silver sulfide at 923 K:[155] $Z = 4$, $a = b = c = 0.62831(8)$ nm

Atom	Position and multiplicity	Atomic coordinates *x*	*y*	*z*	Occupancy
Ag1	8(c)	0.25	0.25	0.25	0.088(7)
Ag2	32(f)	0.303(4)	0.303(4)	0.303(4)	0.15(1)
Ag3	48(i)	0.5	0.381(4)	0.381(4)	0.027(3)
S	4(a)	0	0	0	1

Using the temperature dependences of the crystal lattice parameters of monoclinic acanthite α-Ag_2S, cubic argentite β-Ag_2S, and cubic phase γ-Ag_2S, it is possible to estimate the interatomic distances in these phases at comparable temperatures close to the α-Ag_2S–β-Ag_2S and β-Ag_2S–γ-Ag_2S transformation temperatures. The least distance between the Ag1 and Ag1 atoms in the crystal lattice of monoclinic α-Ag_2S acanthite at 433 K is 0.3351 nm, and the least distance between the Ag1 and Ag2 atoms is in the interval from 0.3085 to 0.3200 nm.[166,173] The covalent diameter of the Ag atom is ~0.292 nm. With that in mind, it is clear that Ag atoms in monoclinic acanthite are at rather large distances from each other and, therefore, occupy their crystallographic sites with a probability ~1. According to,[166,173] in the crystal lattice of cubic β-Ag_2S argentite at 443 K, the least possible distance between the Ag1 and Ag1 atoms is 0.2428 nm, between the Ag1 and Ag2 atoms is from 0.0927 to 0.2971 nm, and between the Ag2 and Ag2 atoms is from 0.0988 to 0.2998 nm. Thus, in cubic argentite, the possible distances between Ag atoms are too small for the 6(b) and 48(j) positions to be occupied by Ag atoms with a probability of 1. Indeed, the occupancies of the 6(b) and 48(j) positions by Ag atoms in β-Ag_2S (in other words, the probabilities of finding Ag atoms in the 6(b) and 48(j) sites) are very small and equal to ~0.0978 and ~0.0711, respectively. In the cubic γ-Ag_2S phase, the possible distances between Ag atoms are too small for the 8(c), 32(f) and 48(i) positions to be occupied by Ag atoms with a probability of 1. Therefore, the probabilities of filling of the 8(c), 32(f) and 48(i) sites by Ag atoms are <0.1. Physically, this means that Ag atoms in the lattices of cubic β-Ag_2S and γ-Ag_2S phases are in constant motion over all possible crystallographic positions. It is this constant motion of Ag atoms that provides the stability of crystal lattices of cubic β-Ag_2S and γ-Ag_2S phases, and their superionic conductivity as distinct from the semiconducting α-Ag_2S acanthite.

4. Effect of small particle size on the thermal expansion and heat capacity of Ag_2S

For the application of nanocrystalline Ag_2S in infrared equipment, solar-energy converters and resistive switches, it is necessary to have information about the variation in the thermal expansion coefficient of different Ag_2S phases *versus* the temperature, and about the effect of particle size on such lattice properties of Ag_2S as heat capacity and thermal expansion.

According to,[169] the linear thermal expansion coefficient α_{ac} of acanthite is $\sim 20 \times 10^{-6}$ K^{-1}. According to,[174] in the temperature range 293–450 K, the α_{ac} of bulk acanthite is 16.8×10^{-6} K^{-1}, and the linear thermal expansion coefficient α_{arg} of bulk argentite is 45.8×10^{-6} K^{-1} from ~460 to 570 K.

A systematic *in situ* study of the thermal expansion of coarse-crystalline and nanocrystalline powders of Ag_2S in the region of existence of monoclinic α-Ag_2S acanthite and cubic β-Ag_2S

argentite has been done for the first time in works[166,173] *via* a high-temperature XRD method. Recently, direct dilatometric measurements of the thermal expansion of coarse-crystalline and nanocrystalline Ag_2S at 290 to 970 K in the region of existence of monoclinic acanthite α-Ag_2S, argentite β-Ag_2S, and γ-Ag_2S phases, as well as the heat capacity of nanocrystalline Ag_2S in the temperature interval from 300 to 930 K, have been carried out in study.[175]

The average particle size in coarse- and nanocrystalline Ag_2S powders was ~430 and ~66 nm.

The effect of temperature on the evolution of XRD patterns of nanocrystalline Ag_2S is shown in Fig. 14. The XRD patterns of Ag_2S recorded at <450 K contain the diffraction reflections of monoclinic (space group $P2_1/c$) acanthite α-Ag_2S, and the XRD patterns recorded at >450 K contain the diffraction reflections of cubic (space group $Im\bar{3}m$) argentite β-Ag_2S. Thus, a polymorphous phase transformation of monoclinic acanthite α-Ag_2S into bcc argentite β-Ag_2S takes place at ~448–453 K.

According to data from high-temperature XRD studies,[166,173] the isotropic (averaged in all crystallographic directions) linear thermal expansion coefficient $\alpha_{\text{ac-nano}}$ of nanocrystalline acanthite in the temperature range 300–400 K is

$$\alpha_{\text{ac-nano}}(T) = 13.4 \times 10^{-6} + 2.7 \times 10^{-8}T \pm 2 \times 10^{-6}\ [\mathrm{K}^{-1}]. \quad (7)$$

The $\alpha_{\text{ac-nano}}$ of nanocrystalline acanthite is ~25% larger than the analogous coefficient α_{ac} of coarse-crystalline acanthite. The difference in the coefficients $\alpha_{\text{ac-nano}}$ and α_{ac} is due to the small particle size in nanocrystalline acanthite. Earlier, a similar difference in the linear thermal expansion coefficients of nanocrystalline film and coarse-grained sample was observed for PbS.[4,176,177]

According to,[166,173] the dependence of α_{arg} on the annealing temperature T in the range 443–623 K can be represented as

$$\alpha_{\text{arg}}(T) = 84.5 \times 10^{-6} - 6.9 \times 10^{-8}T \pm 3 \times 10^{-6}\ [\mathrm{K}^{-1}]. \quad (8)$$

The temperature dependences of $\alpha_{\text{aver}}(T)$ for coarse- and nanocrystalline Ag_2S measured by dilatometry are demonstrated in Fig. 18. The largest coefficient $\alpha_{\text{aver}}(T)$ in the examined temperature range 293–970 K belonged to nanocrystalline Ag_2S produced from a powder with an average particle size of ~66 nm. The average linear thermal expansion coefficients α_{aver} of coarse-crystalline and nanocrystalline acanthite α-Ag_2S and argentite β-Ag_2S measured in works[166,173] by high-temperature XRD are shown in Fig. 18 for comparison. The results of dilatometric and high-temperature XRD measurements of α_{aver} agree with each other satisfactorily.

The heat capacity of Ag_2S nanopowder changes monotonically with rising temperature, except for the transition regions (Fig. 19). In the temperature range 300–450 K, the heat capacity increases and then, near the transition temperature $T_{\alpha\text{-}\beta}$, it experiences a discontinuity. In the region of existence of the β-Ag_2S phase, in the temperature interval from ~470 to ~840 K, the heat capacity first decreases slightly to ~670 K and then grows slightly to the transition temperature $T_{\beta\text{-}\gamma}$, where it discontinues. As the temperature increases further to ~890 K, a small reduction of the heat capacity is observed and, at $T > 890$ K, the heat capacity increases slightly. According to the heat capacity measurements, the transition temperatures $T_{\alpha\text{-}\beta}$ and $T_{\beta\text{-}\gamma}$ were 451 and 858 K, respectively.

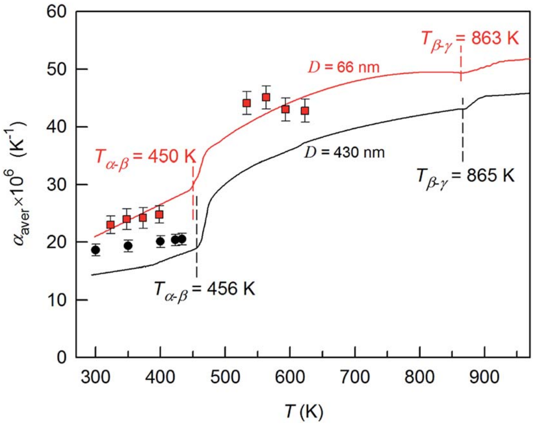

Fig. 18 The average thermal expansion coefficients α_{aver} of coarse- and nanocrystalline silver sulfide measured by dilatometry in the temperature range 293–970 K. The thermal expansion coefficient α_{aver} of coarse-crystalline (●) and nanocrystalline (🟥) silver sulfides measured in works[166,173] by the high-temperature XRD method are shown for comparison. The discontinuity regions of the coefficient $\alpha(T)$ are shown by a dotted line. Reproduced from ref. 175 with permission of Springer.

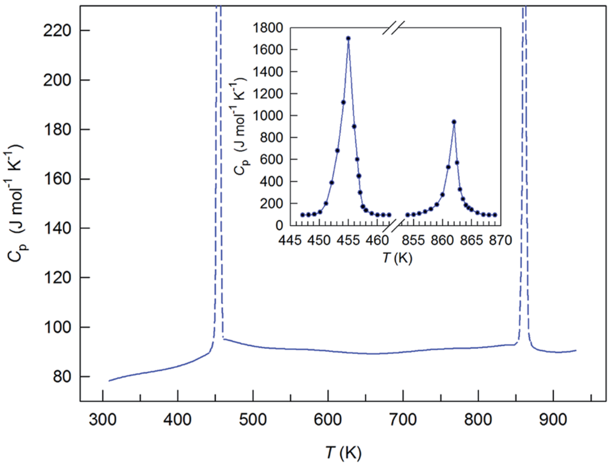

Fig. 19 Heat capacity of silver sulfide nanopowder. The inset shows the spasmodic change of C_p for Ag_2S nanopowder in the regions of α-Ag_2S–β-Ag_2S and β-Ag_2S–γ-Ag_2S transformations. Reproduced from ref. 175 with permission of Springer.

The peaks of the heat capacity C_p of Ag_2S nanopowder in the α-Ag_2S–β-Ag_2S and β-Ag_2S–γ-Ag_2S transformation regions were symmetric rather than λ-shaped (Fig. 19, inset). A symmetric shape of the observed peaks is more characteristic of first-order phase transitions. The heat capacity peaks were very narrow (the width of peak base was about 8 K), which is also typical for first-order phase transitions.

The enthalpy of the phase transformations α-Ag_2S–β-Ag_2S and β-Ag_2S–γ-Ag_2S was estimated to be $\Delta H_{\alpha\text{-}\beta} = 4.2 \pm 0.4$ and

$\Delta H_{\beta-\gamma} = 1.2 \pm 0.3$ kJ mol^{-1}, respectively. According to data,[167,168,170] the enthalpy $\Delta H_{\alpha-\beta}$ is 3.98, 3.93, and 4.06 kJ mol^{-1}, respectively. According to,[162,165,166] the enthalpy $\Delta H_{\alpha-\beta}$ is 3.7–3.9 kJ mol^{-1}. As reported in,[168,170] the enthalpy $\Delta H_{\beta-\gamma}$ of the transformation of argentite β-Ag_2S into the γ-Ag_2S phase was ~0.50 and ~0.78 kJ mol^{-1}, respectively. Within the measurement error, the obtained values of enthalpies $\Delta H_{\alpha-\beta}$ and $\Delta H_{\beta-\gamma}$ were close to the literature data.

For comparison, Fig. 20 presents experimental data on the heat capacity C_p of nanocrystalline Ag_2S[175] and the most reliable experimental data from the literature on the C_p of coarse-grained Ag_2S[170] obtained with the use of adiabatic-shell calorimetry. In the whole temperature region, the heat capacity of nanocrystalline Ag_2S measured in study[175] was 1–4% larger than the heat capacity of coarse-crystalline sulfide.[170] The measured heat capacity C_p peaks of Ag_2S nanopowder was slightly broadened in temperature as compared with those for bulk Ag_2S obtained in study.[170]

The main reason of variation of the lattice properties of nanocrystals in comparison with bulk substances is variation of the shape and boundaries of the phonon spectrum, *i.e.* change of the frequency distribution function of atomic vibrations.[176]

According to,[178,179] waves can occur in nanoparticles whose length does not exceed the doubled maximum size of the particle D, *i.e.*, $\lambda \le 2D$. Hence, on the side of low-frequency vibrations, the phonon spectrum is limited by a certain minimal frequency $\omega_{\min} \geq 2\pi \frac{c_t}{2D}$, where c_t is the velocity of propagation of transverse elastic vibrations (*i.e.*, transverse velocity of sound). In bulk crystals, there is no limitation like this. Besides, the phonon spectrum is limited on the side of high frequencies.

Studies,[176,177] took into consideration the restrictions of the phonon spectrum of the small particles and used the approach[180] for the upper boundary $\omega_{\max}$ of the phonon spectrum of small particles. They showed that the molar heat capacity of a model nanocrystalline substance with particles of a cubic shape with edges in length D can be presented as a function not only of the temperature T, but also of the size D of the small particle:

$$C_V(T,D) = C_V^{\text{bulk}}(T) + n\left(\frac{12\nu_m k_1 T}{D^2} + \frac{6\nu_m k_2 T^2}{D}\right), \tag{9}$$

where the first summand represents the Debye heat capacity of bulk crystal in the low-temperature region. The values $k_1 = (k_B{}^2 c_1{}^{-1}/8\pi\hbar)I_2$ and $k_2 = (k_B{}^3 c_2{}^{-1}/2\pi\hbar^2)I_3$ are positive constants, including the Riemann zeta functions and effective propagation velocities of elastic vibrations, $c_1{}^{-1}$ and $c_2{}^{-1}$.

The linear thermal expansion coefficient $\alpha(T)$ is related to heat capacity C_V by the known relationship

$$\alpha(T) = \frac{\gamma}{3B}\frac{C_V(T)}{\nu_m}, \tag{10}$$

where B is the bulk modulus, ν_m is the molar volume, and γ is the Grüneisen constant.

With allowance for eqn (9) and (10), the thermal expansion coefficient of nanocrystalline substance can be presented as

$$\alpha(T,D) = \alpha_{\text{bulk}}(T) + n\frac{\gamma}{3B}\left(\frac{12k_1 T}{D^2} + \frac{6k_2 T^2}{D}\right). \tag{11}$$

Thus, the heat capacity and the thermal expansion coefficient of a nanocrystalline substance include an additional positive contribution as compared with the same properties of a coarse-grained (bulk) substance. Exactly this result was observed for the heat capacity and the thermal expansion coefficient of nanocrystalline and coarse-grained (bulk) Ag_2S. The appearance of a positive contribution is due to the restriction of the phonon spectrum on the side of low and high frequencies.

According to,[166] the reduction of the particle size in Ag_2S is accompanied by enhancement of the anharmonicity of atomic vibrations. Anharmonicity results in enhanced phonon–phonon scattering, which reduces the thermal conductivity κ and increases the ZT of nanostructured Ag_2S. This confirms the possibility of application of nanostructured Ag_2S as a thermoelectric material that it was noted in study.[58]

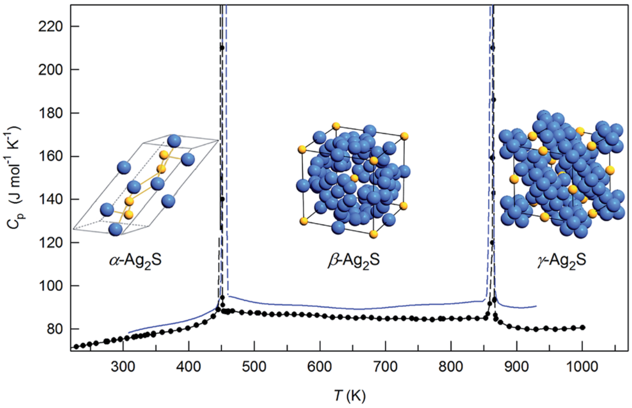

Fig. 20 Heat capacity of silver sulfide nanopowder. For comparison, the heat capacity (●) of coarse-grained Ag_2S[170] is shown. The unit cells of α-Ag_2S acanthite, β-Ag_2S argentite and γ-Ag_2S phase are shown in the temperature regions of existence of these phases. Reproduced from ref. 175 with permission of Springer.

5. Heteronanostructures based on Ag_2S

Semiconductor–metal hybrid heteronanostructures may exhibit not only a combination of properties of the separate components but also further enhanced property tunability. It is supposed that, owing to synergetic effects, new improved properties will arise from the interactions between the metal and semiconductor.

Among semiconductor–metal nanocomposites, the heteronanostructures based on Ag_2S have attracted special attention and are very useful for manifold applications. Ag_2S-based heteronanostructures can be used in infrared detectors, in resistance-switches and nonvolatile memory devices, and for bioimaging as biomarkers.[2,5,16,43,48–50,181–183] According to,[184,185]

Ag_2S-based heteronanostructures exhibit an excellent bactericidal effect against many types of bacteria. In recent years, Ag_2S-based semiconductor–metal heterostructures have emerged as one of the leading materials for photocatalytic conversion of sunlight energy.[186–188]

Synthesis of Ag_2S/M (M = Ag, Au, Pt, Pd, Os) heteronanostructures was studied in detail by Yang, Ying and co-authors.[16,40,189,190] They developed a general scheme for transferring the transition metal ions from water to an organic medium using an ethanol-mediated route, which was extended to preparation of a variety of semiconductor/noble-metal heteronanostructures.

A room-temperature method was developed to first derive aqueous-dispersible Ag_2S nanocrystals. Typically, $C_{18}H_{17}K_2O_8PS_2$ salt was added to aqueous $AgNO_3$ solution. The mixture was stirred for 1 h to form Ag-complexes, with subsequent prompt addition of aqueous Na_2S solution, which resulted in Ag_2S hydrosol being produced.[40] Then, Ag_2S nanocrystals were used as seeds for the formation of nanocomposites with different metals. By using 7 nm Ag_2S nanocrystals, Na_3Cit, and various noble-metal precursors at 378 K (for gold) and 383 K (for other noble metals), a set of Ag_2S/M heteronanostructures were obtained, such as Ag_2S/Au and Ag_2S/Ag (Fig. 21), Ag_2S/Pt, Ag_2S/Os, and Ag_2S/Pd. In the presence of Ag_2S seeds, the metals nucleated preferentially on the existing Ag_2S seeds rather than homogeneously.

Cation-exchange reactions can also be used to prepare heteronanostructures through the partial transformation of ionic nanocrystals.[2]

The chemical transformation of nanocrystalline solids has emerged as a very promising strategy for inorganic nanostructure synthesis. Among various chemical transformations, the cation-exchange reaction is especially interesting because it can alter the composition of the existing ionic nanocrystal by replacing the cations within the crystal lattice with a different metal ion.

The cation exchange at the nanoscale can transfer one material into another while retaining its morphology. If the exchange only takes place partially in the nanostructure, alloy or core–shell structures are formed. However, by carefully controlling the reaction, heterostructures may also be obtained. Alivisatos and co-authors[191] gave an example of partial change of CdS nanorods into Ag_2S to form CdS–Ag_2S superlattices. CdS nanorods in toluene were added to a solution containing toluene, $AgNO_3$ and methanol at very low temperature and then warmed to room temperature slowly to allow the replacement reaction. The lattice mismatch strains induced the spontaneous formation of periodic structures. The product showed an array of Ag_2S quantum dots separated by confining regions of CdS. Such an array has potential applications as nanometer-scale optoelectronic devices.

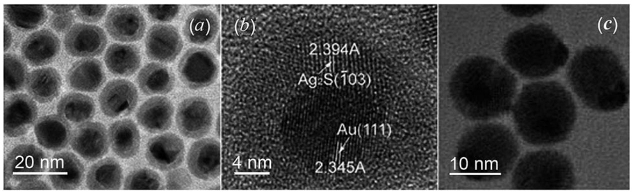

Fig. 21 (a) TEM and (b) HRTEM images of Ag_2S/Au heteronanostructures,[188] and (c) TEM image of Ag_2S/Ag heteronanostructures.[16]

Ag_2S/ZnS heteronanostructures having a matchstick shape with Ag_2S quantum dots as the heads and ZnS quantum rods as the stems were synthesized in study.[192] These hybrid quantum rods were synthesized by a one-pot thermal decomposition method, and their size could be tuned by changing the ratio between the Ag–DDTC and zinc diethyldithiocarbamate (Zn $[S_2CN(C_2H_5)_2]_2$ or $Zn(DDTC)_2$) precursors. The diameter of the Ag_2S head in the Ag_2S/ZnS heterostructures was around 8.5 nm and the stem size was ~7.8 × 35 nm when a 1 : 2 Ag(DDTC) : $Zn(DDTC)_2$ molar ratio was used in the synthesis. With an increased molar ratio of 2 : 1, the diameter of the Ag_2S head in the heteronanostructures was about 4.5 nm and the stem size was ~4 × 48 nm (Fig. 22). The Ag_2S/ZnS heteronanostructures exhibited appealing PL in UV/blue and NIR regions. Later, Shen *et al.*[43] modified the synthetic approach to demonstrate one-pot fabrication of Mn-doped Ag_2S/ZnS quantum rods with multicolor PL in three wavelength regions (blue, orange, and NIR).

A convenient room-temperature method for preparation of a new type of Ag_2S/Ag heterodimers was devised in study.[55] At first, monodisperse CdS colloidal nanospheres were synthesized through a modified polyol process (*i.e.*, synthesis of

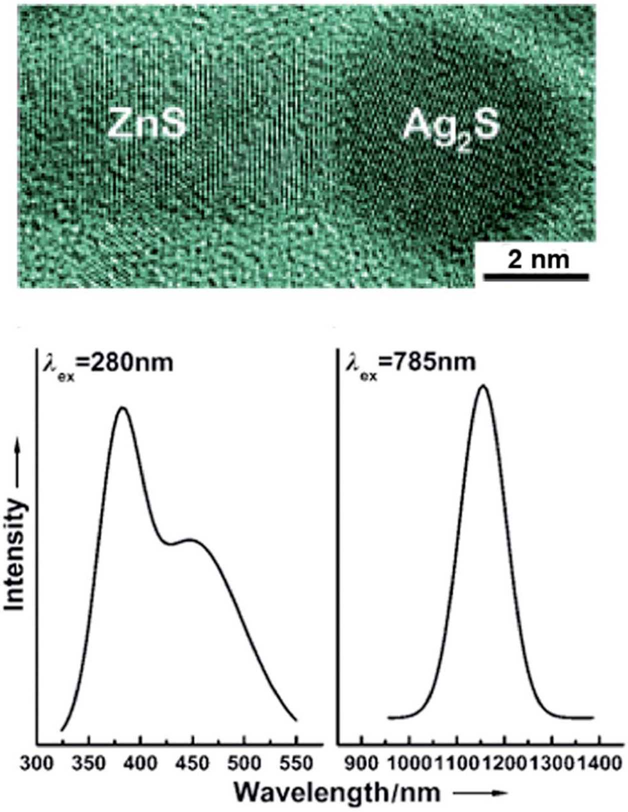

Fig. 22 HRTEM image of an Ag_2S/ZnS heteronanostructure and its UV/blue and NIR photo-luminescence at 280 and 785 nm, excitation, respectively. Reproduced from ref. 192 with permission from Wiley.

a metal-containing compound in PEG). The CdS nanospheres were used as solid precursors for subsequent chemical transformation to Ag_2S nanospheres *via* cation exchange and as a template for deposition of metallic silver. As a result, each Ag_2S nanosphere was grown with a triangular prism of a Ag crystal, leading to formation of a novel type of asymmetric semiconductor/metal photosensitive heterodimers. According to,[55] these Ag_2S/Ag semiconductor/metal heterodimers exhibited remarkable bactericidal activity under visible-light illumination and may find future applications, including bacterial deactivation, bioimaging and sensing, as well as heterogeneous catalysis under ambient conditions.

According to study,[193] mono-dispersed Ag_2S@Ag hybrid nanocomposites exhibit superior adsorption performance for the removal of such organic contaminants as methyl blue and methyl orange from wastewater. Mono-dispersed Ag_2S@Ag nanoparticles have been synthesized using laser ablation of bulk Ag targets in activated aqueous solution containing C_2H_5NS and hexadecyl trimethyl ammonium bromide.

Comparison of the advantages and disadvantages of the main methods for synthesis of Ag_2S/Ag heteronanostructures is presented in Table 5.

Nonvolatile memory unit represents one of the most important components in state-of-the-art microelectronic/nanoelectronic devices and has been subject of intensive investigations in the past decades.[16,48–50,181,194] Among different concepts memories, resistive switching memories, whose operation is primarily based on ion migrations that can result in reversible formation and breakage of a conductive filament in the sandwiched metal–insulator–metal structure, are particularly intriguing because they have a low production cost, offer reduced power consumption, and a switching rate as fast as semiconductor devices currently used and, in principle, can be made arbitrarily small. The Pt/Ag_2S/Ag is an interesting structure exhibiting well-defined resistive switching behavior.[181] For example, Aono and co-authors[181,195] demonstrated basic logic gate operations and fabricated a 1 kbit nonvolatile memory chip based on a Pt/Ag_2S/Ag heteronanostructure. Recently, they further clarified the rate-limiting processes determining the switching time in a Pt/Ag_2S/Ag system, thus providing a deeper understanding toward the switching mechanism.[196] Despite much recent progress, for future applications, an extended array of Ag_2S/Ag resistive switches with smaller feature size as well as compatibility with conventional Si-based technology would be more favorable, but has not been realized.

The semiconductor/metal Ag_2S/Ag heteronanostructures are interesting for the production of resistive switches and nonvolatile memory devices.

The electrical properties of Ag_2S/Ag heteronanostructure of the heteronanowire type have been studied in work.[48] An anodic aluminum oxide (AAO) template-assisted electrochemical strategy was used for synthesizing a Ag_2S/Ag heteronanowire array. The porous AAO membrane was deposited partially with Ag nanowires, and then Ag_2S nanowires were grown by electrochemical sulfurization. Liang *et al.*[48] assumed that the main reason for the resistance-switching phenomenon in this Ag_2S/Ag heteronanostructure was the creation and dissolution of a filament-like Ag conducting bridge.

Recently, authors of study[194] reported the fabrication of an extended array of Ag_2S/Ag nanodots with a density of 60 Gbit in^{-2}, which was accomplished by sputtering Ag onto a Si substrate using an ultrathin porous AAO membrane as a shadow mask, followed by room-temperature sulfurization (Fig. 23). This resulted in the formation of a high density of Ag_2S/Ag bilayer nanodots with a feature size of 45 nm.

The resistance switching behavior of an Ag/Ag_2S/W nanoscale heterostructure of sandwich type was studied by Xu *et al.*[49] To synthesize Ag_2S, an Ag wire of diameter of 0.5 mm heated with S powder to 470 K for 30 min. The sulfidized Ag wire was scratched by an Ag wire so that some small pieces of Ag_2S were transferred to the Ag wire. For observation, the Ag wire with the Ag_2S tip-end was mounted on a high-resolution transmission electron microscope opposite the sharp tungsten W tip. Xu *et al.*[49] directly observed the formation and breakage of a conducting pathway in a superionic solid electrolyte resistance

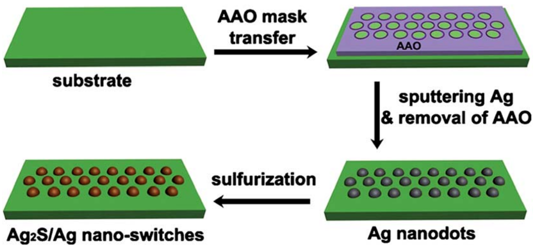

Fig. 23 Schematic illustration of the fabrication of Ag_2S/Ag nanodot resistive switch arrays (AAO is anodic aluminum oxide).[194]

Table 5 Main methods of synthesis of Ag_2S/Ag heteronanostructures

Method	Main reagents^a	Advantages	Disadvantages	Ref.
Hydrothermal cation exchange	$AgNO_3$, Na_2S, Na_3Cit, $C_{18}H_{17}K_2O_8PS_2$	Controllable size	Complicated process	40, 189 and 190
Cation exchange	$Cd(NO_3)_2$, $AgNO_3$, Na_3Cit, $(NH_2)_2CS$, C_2H_5OH, C_3H_6O, PVP	Controllable size	Complicated sequential process	55
Laser ablation	Ag, C_2H_5NS, $C_{16}H_{33}N(CH_3)_3Br$	Controllable size	Complicated operation, high cost	193
Hydrochemical deposition	$AgNO_3$, Na_2S, Na_3Cit	Controllable size, non-toxic reagents, safety	Low yield	195 and 200

[a] PVP – polyvinylpyrrolidone $(C_6H_9NO)_n$.

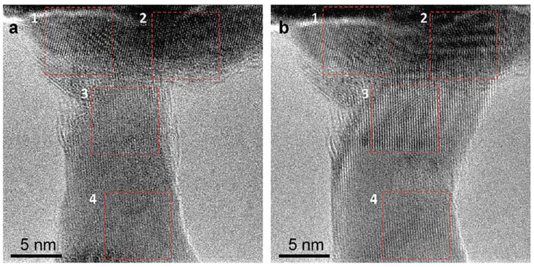

Fig. 24 (a) Off- and (b) on-states of a narrow and thin Ag_2S/Ag device regions. The Ag electrode is located on the top part of the image, and the W electrode is in the bottom part. When the device is switched from the off- to on-states, an area 1 has almost no change, the argentite appears in area 2, the argentite and Ag appear in area 3, and no changes are seen in area 4. Reproduced from ref. 49 with permission from ACS.

nanoswitch with complete reproduction of its performance (Fig. 24). They found that the transition of semiconducting acanthite α-Ag_2S into conducting argentite β-Ag_2S took place at room temperature and only within a conductive pathway. The argentite not only formed part of the conducting channel but also provided the pathway for the migration of Ag^+. In fact, the Ag^+ could migrate only in the argentite phase and not in the acanthite α-Ag_2S phase.

In study,[197] a wet chemical process was used for fabrication of Ag_2S flat thin films on Ag electrodes utilized for an atomic Ag_2S/Ag switch. A counter electrode made of Ag with a gap of ~1 μm was fabricated using conventional UV-lithography on a Si substrate. The substrate with Ag was dipped into an aqueous solution of Na_2S for sulfurization. As a result, Ag_2S was formed on the Ag surface.

In study,[50] the resistive switches Ag_2S/Ag nanoclusters for memory cells were formed by sulfurization of melting-dispersed thin continuous Ag films. Ag nanocluster arrays were formed by thermal annealing of 10 nm-thick Ag films at 500 K during 40 min immediately after vacuum thermal evaporation. Low-temperature sulfurization in a H_2S atmosphere in an airtight chamber was used to obtain Ag_2S particles.

Gubicza *et al.*[198] demonstrated stable resistive switchings in metallic Ag–Ag_2S–Ag heteronanojunctions created by an scanning tunneling microscope (STM). An 80 nm-thick Ag layer was deposited onto a Si substrate followed by a 5 min sulfurization in a H_2S atmosphere at 333 K. As a result, a 30 nm-thick stoichiometric Ag_2S cap layer on the planar Ag electrode was obtained. Nanometer-scale junctions were created between the Ag_2S surface and a mechanically sharpened Ag wire of 0.35 mm in diameter in STM geometry. According to,[198] fast and highly integrable memory cells are the merits of lithographically designed Ag–Ag_2S–Ag heteronanostructures.

The synthesis of multifunctional nanocomposite systems is of great interest. In particular, heteronanostructures such as Ag_2S/Ag consisting of a semiconductor and a noble metal are very useful for various applications. This type of heterostructures that contain Ag and Ag_2S nanowires or an Ag film with Ag_2S/Ag nanoclusters are considered for the production of biosensors,[183] resistive switches, and nonvolatile memory devices.[48–50,194,197,199] The action of the resistive switch is based on the phase transformation between nonconducting α-Ag_2S acanthite and superionic β-Ag_2S argentite.

Hydrochemical deposition has been applied for the first time to the synthesis of Ag_2S/Ag heteronanostructures in studies.[136,200–203] Ag_2S/Ag heteronanostructures have been synthesized by chemical deposition from aqueous solutions of $AgNO_3$, Na_2S, and Na_3Cit with a reduced concentration of Na_2S ($C_{Na_2S} < C_{AgNO_3}/2$). Synthesis was carried out under illumination of solutions by a light-emitting diode with a 450 nm wavelength and an irradiation intensity of 15 mW cm^{-2}. Two processes take place simultaneously in such mixtures: formation of Ag_2S and appearance of Ag nanoparticles as a result of photochemical reduction reaction (6) of Ag^{2+} by $C_6H_5O_7{}^{3-}$. At certain synthesis conditions, Ag and Ag_2S nanoparticles are united in Ag_2S/Ag nanocomposites.

The scheme of deposition of Ag_2S/Ag heteronanostructures from aqueous solutions of $AgNO_3$, Na_2S and Na_3Cit, TEM and HRTEM images of Ag_2S, Ag and Ag_2S/Ag particles and their diffraction patterns, as well as EDX analysis of Ag_2S, Ag particles and Ag_2S/Ag heteronanostructures are shown in Fig. 25.

Synthesis was carried out in a particular sequence. Briefly, a complexing agent was added to $AgNO_3$ in the dark. Then, a solution of Na_2S was poured into the prepared solution (Fig. 25a). As a result, deposition of Ag_2S powder occurred. Then, the solution was irradiated with monochromatic light at wavelength 450 nm. In accordance with the photochemical reaction (6) $C_6H_5O_7{}^{3-}$ reduced the Ag^+ to Ag nanoparticles in aqueous solutions (Fig. 25b). The reduction of Ag at the surface of Ag_2S nanoparticles leads to the formation of Ag_2S/Ag heteronanostructures (Fig. 25c).

The HRTEM images of deposited Ag_2S, Ag and Ag_2S/Ag particles are shown in Fig. 25d–f, respectively. In studies,[136,200,201,203] the diffraction patterns (selected area of electron diffraction (SAED)) (Fig. 25g–i) of these particles were obtained by fast Fourier transformation (FFT) of their HRTEM images.

The observed set (Fig. 25g) of diffraction reflections and interplanar distances of Ag_2S nanoparticles corresponded to monoclinic (space group $P2_1/c$) nanocrystalline acanthite α-$Ag_{1.93}S$.[148] The Ag nanoparticle (Fig. 25e) had a cubic (space group $Fm\bar{3}m$) structure with microtwinning in the direction of the [111] planes (Fig. 25h). Diffraction patterns (Fig. 25i) obtained by FFT of HRTEM images (Fig. 25f) of Ag_2S/Ag heteronanostructures revealed reflections of monoclinic Ag_2S and twinned reflections of cubic Ag.

According to the EDX results (Fig. 25j–l), the content of Ag and S in Ag_2S nanoparticles was ~86.3 ± 0.4 and ~12.9 ± 0.1 wt% and corresponded to ~$Ag_{1.95-1.98}S$. Ag nanoparticles contained Ag only, and Ag_2S/Ag heteronanostructure contained about 87.8 and 11.5 wt% of Ag and S, respectively.

The XRD pattern and HRTEM images of Ag_2S/Ag heteronanostructures are shown in Fig. 26. Areas (1) and (3) correspond to Ag and Ag_2S nanoparticles, respectively. The Ag nanoparticle clearly exhibited microtwinning in the direction of the [01−1] planes. Area (2) corresponded to that part of heteronanostructure where the Ag_2S and Ag nanoparticles are in

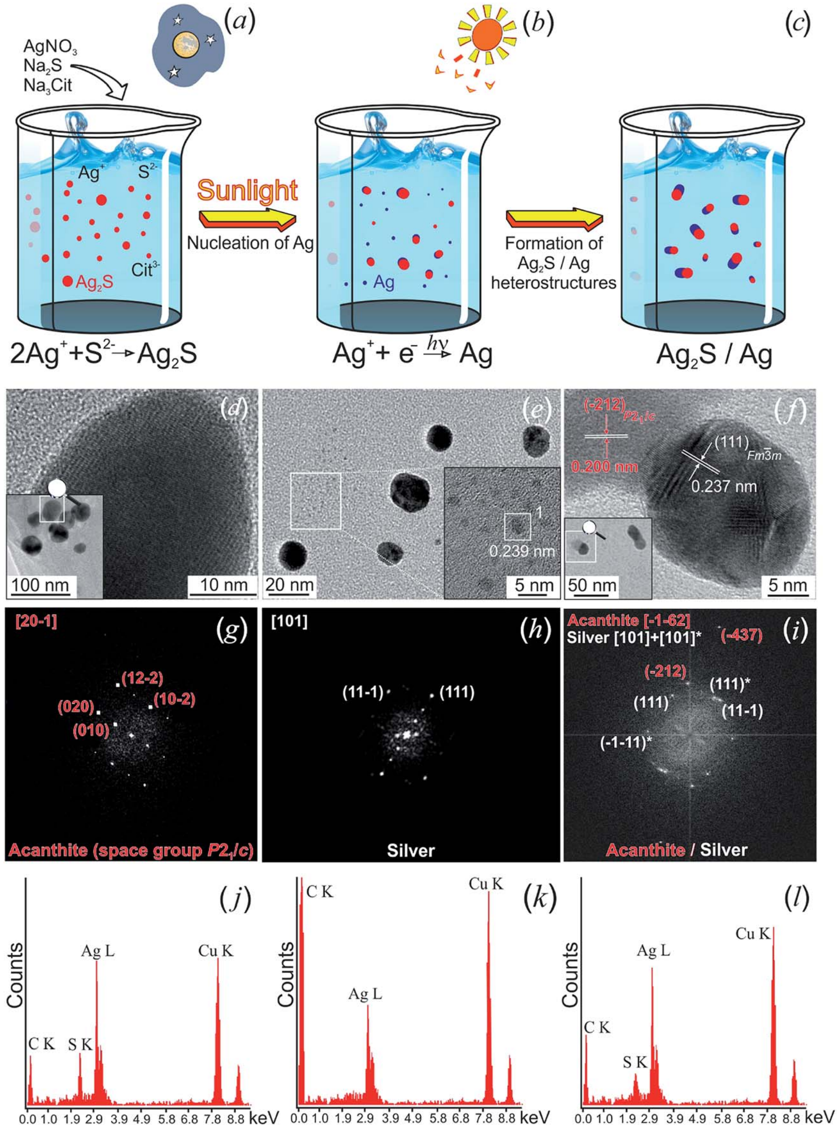

Fig. 25 Hydrochemical bath deposition of Ag_2S/Ag heteronanostructures. (First row) scheme of deposition. (Second row) TEM and HRTEM images of (d) Ag_2S nanoparticles, (e) Ag nanoparticles, and (f) Ag_2S/Ag heteronanostructures. (Third row) FFT patterns (g), (h), and (i) obtained from the (d), (e), and (f) HRTEM images, respectively. (Fourth row) EDX analysis of (j) Ag_2S nanoparticle, (k) Ag nanoparticle, and (l) Ag_2S/Ag heteronanostructure. Reproduced from ref. 200 with permission of Springer.

direct contact. Indeed, a set of spots (Fig. 26b) contains diffraction reflections of both phases: Ag_2S and Ag. The interplanar distances for area (3) and the set of eight spots (Fig. 26c) corresponded to monoclinic (space group $P2_1/c$) α-Ag_2S acanthite.

The Ag_2S/Ag heteronanostructures combine ionic and electronic conductors and can be used to create biosensors, resistive switches and nonvolatile memory devices.

Let us turn to a discussion of Ag_2S/Ag heteronanostructures prepared by the hydrochemical deposition method.

A typical Ag_2S/Ag heteronanostructure contained in the colloidal solution prepared from aqueous solutions of $AgNO_3$, Na_2S and Na_3Cit is shown in Fig. 27 as an example. As can be seen, the Ag_2S and Ag nanoparticles are in immediate contact. The Ag nanoparticle clearly exhibits microtwinning in the direction of the [111] planes. According to the EDX data, the nanoparticle contains only Ag. The interplanar distances observed for Ag_2S nanoparticles correspond to monoclinic acanthite. The zone axis of the Ag_2S nanoparticle matrix is $[101]_{P2_1/c}$.

The resistive switches of Ag_2S/Ag types consist of a superionic conductor located between two metal electrodes. In the case of Ag_2S/Ag heterostructures, one of the electrodes is Ag, and the second electrode can be Pt, Au, Cu, or W. The conductivity of Ag was 6.3×10^5 ohm^{-1} cm^{-1}, that of the β-Ag_2S argentite and α-Ag_2S acanthite phases were about 1.6×10^3 and only 2.5×10^{-3} ohm^{-1} cm^{-1} at room temperature,[35] respectively. Thus, the conductivity of acanthite was 6 orders of magnitude lower than that for the argentite phase. It is, thus, reasonable to conclude that the conducting channel in Ag_2S/Ag heterostructures can be made of a mixture of Ag and β-Ag_2S argentite.

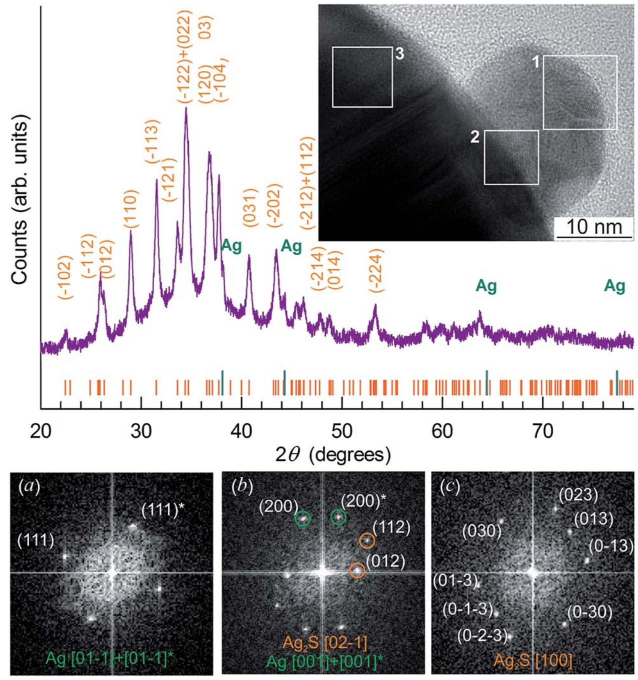

Fig. 26 The XRD pattern and HRTEM image of Ag_2S/Ag heteronanostructures. The long and short ticks on XRD patterns correspond to reflections of cubic metallic Ag and monoclinic Ag_2S, respectively. The areas (1) and (3) isolated by a white square correspond to Ag and Ag_2S, respectively. Area (2) corresponds to the region where the Ag_2S and Ag nanoparticles are in direct contact. (a), (b), and (c) Selected areas of electron diffraction obtained by FFT of areas (1), (2), and (3) of heteronanostructure. Twinned reflections of silver are marked by *. Reproduced from ref. 200 with permission of Springer.

In studies,[136,200–203] Ag_2S/Ag heteronanostructures formed by Ag_2S and Ag nanoparticles were produced by a simple method of hydrochemical bath deposition. Deposition of Ag_2S/Ag heterostructures on a substrate coated with a thin conducting metallic layer will make it possible to form a structure that can work as a resistive switch. The action of the switch is based on the phase transformation of nonconducting α-Ag_2S acanthite into β-Ag_2S argentite exhibiting superionic conduction. The transition into a high-conduction state is due to abrupt disordering of the cationic sublattice. Authors of studies[204,205] have shown that a high-conduction state of a crystal can be achieved by external electric field-induced "melting" of the cationic sublattice taking place without heating of the crystal. Such transformation occurring as a result of applied external electric field was confirmed with respect to nanocrystalline Ag_2S in studies.[49,50,194,199] The effect of an external electric field induced abrupt disordering, allowing the realization of the superionic state of Ag_2S at room temperature. This opens up the possibilities for the practical use of materials based on Ag_2S.

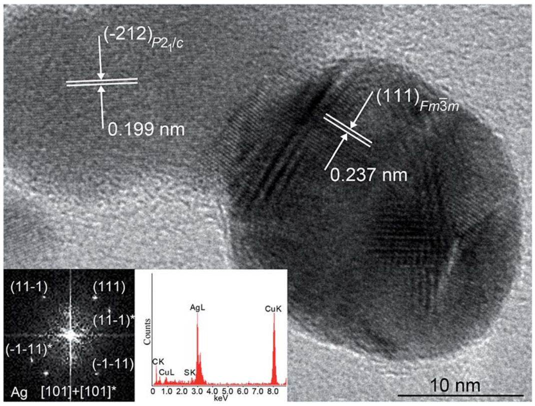

Fig. 27 HRTEM image of Ag_2S/Ag heteronanostructures. Monoclinic (space group $P2_1/c$) Ag_2S nanoparticle with an α-Ag_2S acanthite structure (upper left corner) is in direct contact with a cubic (space group $Fm\bar{3}m$) Ag nanoparticle. The electron diffraction pattern obtained by FFT of the HRTEM image of an Ag nanoparticle, and cumulative elemental EDX pattern of this Ag nanoparticle, are shown (lower left corner). Twinned reflections of silver are marked by *, zone axes are [101] + [101]*. Reproduced from ref. 136 with permission from Wiley.

Authors of works[200–203] studied preliminarily the switching processes in Ag_2S/Ag heteronanostructures. For this purpose, a metallic Pt microcontact was supplied to Ag_2S/Ag heteronanostructure and bias voltage was impressed so that the Ag electrode was charged positively. When positive bias voltage increased to 500 mV, the conduction of the heteronanostructure grew and the nanodevice transformed into the conducting state (*i.e.*, the on-state). The bias back to negative values decreased the conduction and the nanodevice transformed into the off-state.

Fig. 28 displays a region of an Ag_2S/Ag heteronanostructure where change of crystal structure at the transition from the off-state (Fig. 28a) to the on-state (Fig. 28b) can be observed. Using FFT of HRTEM images, authors of studies[200,202,203] obtained the selected areas of electron diffraction (SAEDs) (Fig. 28c and d).

The electron diffraction pattern of an Ag_2S/Ag heteronanostructure in the off-state is shown in Fig. 28c. This SAED contains (111), (11−1) spots and twinning reflection (111)* corresponding to cubic (space group $Fm\bar{3}m$) Ag, as well as (2−12) and (030) spots corresponding to monoclinic (space group $P2_1/c$) α-Ag_2S acanthite. The observed angle of 100.3° between (2−12) and (030) spots of monoclinic acanthite coincided within the measurement error with the theoretical value 100.7°. Experimental angles between diffraction spots of cubic Ag coincided with the theoretical values.

Then, a positive bias was applied to the Ag_2S/Ag heteronanostructure to turn it on. HRTEM images of an Ag_2S/Ag heteronanostructure in the on-state and its selected electron diffraction patterns are presented in Fig. 28b and d, respectively. The electron diffraction pattern (Fig. 28d) contains two sets of spots corresponding to cubic (space group $Fm\bar{3}m$) Ag, and cubic (space group $Im\bar{3}m$) β-Ag_2S argentite. The observed angle of 30.1° between the (011) and (112) spots of cubic β-Ag_2S argentite coincides with the theoretical value of 30°.

Thus, the applied bias leads to the appearance of conducting β-Ag_2S argentite instead of nonconducting α-Ag_2S acanthite and the formation of conductive channel from argentite β-Ag_2S and Ag.

The current–voltage *I*(*V*) characteristics of the resistive switches based on Ag_2S/Ag heteronanostructures produced by different methods are presented in studies.[48–50,194,199] As a rule,

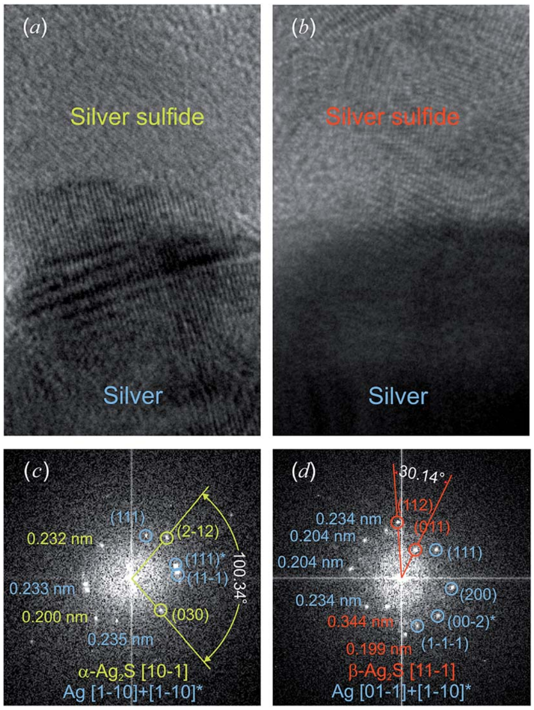

Fig. 28 HRTEM images of the region of transition between Ag and Ag_2S for the (a) off-state and (b) on-state of Ag_2S/Ag heteronanostructures. The on-state arises as a result of applied external positive bias voltage to this Ag_2S/Ag heteronanostructure. The Pt electrode is located on the top part of the image, and the Ag electrode is in the bottom part. Electron diffraction patterns (c) and (d) are obtained by FFT of HRTEM images (a) and (b), respectively. Reproduced from ref. 200 with permission of Springer.

the bias voltage is from ±150 to ±500 mV. According to,[49] the minimum energy barrier for an Ag cation jumping from one atomic site to the other is about 130 meV.

An *I*(*V*) characteristic of the resistive switch based on an Ag_2S/Ag heteronanostructure produced by hydrochemical deposition in studies[200,202,203] is shown in Fig. 29a. The schematic operation of this switch is shown in Fig. 29.

The initial Ag_2S phase was a nonconducting acanthite α-Ag_2S (Fig. 29(1)). When a positive bias was applied, Ag^+ started to move towards the negatively charged cathode M and were reduced to Ag during their transport. Simultaneously, the α-Ag_2S phase transformed into superionic β-Ag_2S argentite (Fig. 29(2)), and a continuous conductive channel was formed (Fig. 29(3)). The continuous conductive channel that was formed from argentite β-Ag_2S and Ag was retained when the external field is turned off. This phenomenon can be considered to be a memory effect (Fig. 29(3)). If a negative (reverse) bias is applied to the switch, the Ag nanocrystals start dissolving in argentite, the Ag^+ move to the anode, argentite transforms into the initial acanthite again, the conductive channel breaks down, and an off-state is realized (Fig. 29(4 and 5)). Because of the formation of nonconducting acanthite, the conductive channel disappears, the switch transforms into the initial state and is turned off (Fig. 29(6)). If positive bias is applied once again, the destroyed conductive channel is restored due to the appearance of argentite and the formation of Ag.

According to,[49,50,202,203] the bias voltage which is sufficient to turn on and turn off the switch is from ±0.2 to ±10.0 V depending on the metal M used as the second electrode.

The UV-vis optical absorption spectra of colloidal solutions containing Ag_2S/Ag composite nanoparticles[200] contain a broad intensive absorption band in the region of ~360 to 450 nm, which corresponds to Ag nanoparticles and is due to surface plasmon resonance (SPR).[55,100,206,207] Also, the weakly diffused absorption peak observed at ~312–320 nm corresponds to Ag_2S nanoparticles.

Ag_2S/Ag nanocomposites can be applied as promising biosensing probes. Ag nanoparticles can be used as biosensors owing to their unique SPR, which depends on the size and shape of particles.[183,208,209] However, Ag nanoparticles are easily oxidized, which is why they should be protected. The combination of Ag nanoparticles and chemically stable Ag_2S allows one to increase the stability of Ag nanoparticles and to use Ag_2S/Ag nanocomposites and $Ag@Ag_2S$ core–shell structures for biosensing applications in the future.

According to,[186,210] Ag_2S/Ag heteronanostructures possess considerable antibacterial activity and can be used in biology and medicine. This agrees with data[54,55,144] on the antibacterial activity of Ag_2S colloidal solutions and nanopowders.

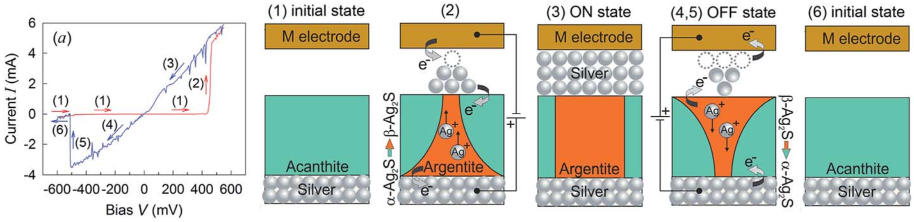

Fig. 29 Generalized scheme of the operation of an Ag_2S/Ag heteronanostructure-based switch: (a) typical current–voltage characteristic of the switching; (1) initial nonconducting state; (2) the appearance of a conductive channel upon the application of an external electric field that induces the transformation of acanthite α-Ag_2S into argentite β-Ag_2S; (3) work on-state with a continuous conductive channel formed from argentite β-Ag_2S and Ag; (4, 5) off-state and breakdown of the conductive channel upon the application of negative bias and the transformation of argentite into initially acanthite; (6) initial nonconducting state after disappearance of the conductive channel and turning-off of the switch. M is the metal electrode. The numbers from 1 to 6 for different states of switching correspond to the order of the events on (a) current–voltage characteristics. Reprinted from ref. 202 with permission from Elsevier.

6. Conclusions and outlook

This review presented the major advances in the controlled synthesis of nanostructured Ag_2S in the form of nanopowders, stable colloidal solutions, quantum dots, isolated nanoparticles with a protective shell, and heteronanostructures. Also, the main results on the study of crystal structure, nonstoichiometry and properties of nanostructured Ag_2S were detailed.

An increasing variety of semiconductor nanostructured Ag_2S with various sizes and shapes can now be prepared. Along with the development of synthetic methods, the applications of nanostructured Ag_2S have become wider.

Investigations over recent years have shown that nanostructured materials based on Ag_2S are more effective than their bulk counterparts due to the following advantages: higher specific surface areas and more active sites for catalysis; longer cycle life; enhanced band gap of the semiconductor Ag_2S phase; higher electric conductivity of high-temperature Ag_2S phases; shorter path lengths for the transport of charge carriers (electrons and holes). Experimental studies of the quantum confinement effect of Ag_2S quantum dots have shown that the exciton diameter of Ag_2S is about 4 nm.

Synthesized forms of nanostructured Ag_2S have several possible applications. First, stable Ag_2S colloidal solutions and Ag_2S quantum dots are suitable for biological and medical application as biomarkers because these solutions are non-toxic and do not contain hazardous substances. Ag_2S quantum dots exhibit bright photoluminescence and excellent photostability. Therefore, Ag_2S quantum dots of size less than 3–4 nm could be used for NIR applications in the biomedical field as luminophores or biomarkers. The creation of a protective shell on Ag_2S quantum dots helps to prevent the agglomeration and growth of quantum dots and to retain their optical properties.

Nanocrystalline Ag_2S powders can be used for production of electronic devices such as photovoltaic cells, photoconductors, and infrared detectors.

Ag_2S/Ag heteronanostructures unite ionic and electronic conductors. A high-conducting state of such heteronanostructures can be induced by an external electric field without heating of this composite owing to phase transformation of nonconducting acanthite into argentite and the exhibition of superionic conduction. Ag_2S/Ag heteronanostructures are intended for application in fast-acting resistive switches and nonvolatile memory devices. Also, Ag_2S/Ag nanocomposites can be applied as promising biosensing probes and photocatalysts. Composite heteronanostructures based on Ag_2S not only combine the properties of the individual nanocrystals, but also lead to new collective properties due to synergetic effects. Recent studies have shown that the synergetic effect can considerably enhance the properties of composite nanomaterials based on nanostructured Ag_2S.

All the forms of nanostructured Ag_2S possess significant potential antibacterial activity, and can be used as effective agents against asepsis and for disinfection.

Thus, recent advances have shown that nanostructured Ag_2S possesses great possibilities for potential application in different areas, from optoelectronics to biomedicine, because of its unique physical and chemical properties and "nanosized" effects.

The exploration and development of new synthetic methods and techniques to prepare nanostructured Ag_2S with better performance, and understanding of its structure-related properties, is an ongoing task for researchers.

Although the last decade has witnessed great progress in the synthesis of nanostructured Ag_2S and its application, challenges still exist. The discussion below illustrates some of the challenges that scientists and technologists are facing in the synthesis and application of nanostructured Ag_2S.

Stable colloidal solutions contain the finest Ag_2S nanoparticles of size about 2–16 nm but the concentration of such nanoparticles is 0.01–0.02 mg mL^{-1} and rather small. That is why an important problem in the synthesis of different forms of nanostructured Ag_2S remains the preparation of more concentrated colloidal solutions that retain their long-term stability and small size of nanoparticles.

Obtaining a narrow size distribution of synthesized Ag_2S nanoparticles (*i.e.*, the synthesis of uniform-sized nanoparticles) is another important challenge. Indeed, the synthesis of monodisperse Ag_2S nanoparticles (with size variation <5%) is of key importance because the properties of the nanoparticles depend strongly on their sizes and uniformity.

One of the major challenges of using Ag_2S quantum dots in electronics is the creation of large arrays of the quantum dots homogeneous in size and shape. The synthesized quantum dots are located on the substrate surface in a random way. For application in electronics, the prepared arrays of Ag_2S quantum dots should be well ordered, preferably by self-organization, and should be compatible with optical devices and detectors. Another important problem facing Ag_2S quantum dot arrays is improvement of the electric conductivity reduced by the organic ligands used in colloidal synthesis. Achieving the necessary performances of Ag_2S quantum dot assemblies is an attainable aim in the next years.

Acknowledgements

This study was supported by the Russian Science Foundation (14-23-00025) *via* the Institute of Solid State Chemistry (Ural Branch) of the Russian Academy of Sciences.

References

1 Z. Zhuang, Q. Peng and Y. Li, *Chem. Soc. Rev.*, 2011, **40**, 5492–5513.

2 M.-R. Gao, Y.-F. Xu, J. Jiang and S.-H. Yu, *Chem. Soc. Rev.*, 2013, **42**, 2986–3017.

3 N. V. Hullavarad, S. S. Hullavarad and P. C. Karulkar, *J. Nanosci. Nanotechnol.*, 2008, **8**, 3272–3299.

4 S. I. Sadovnikov, A. I. Gusev and A. A. Rempel, *Russ. Chem. Rev.*, 2016, **85**, 731–758.

5 G. Xu, S. Zeng, B. Zhang, M. T. Swihart, K.-T. Yong and P. N. Prasad, *Chem. Rev.*, 2016, **116**, 12234–12327.

6 *Semiconductor Nanostructures*, ed. D. Bimberg, Springer, Berlin, Heidelberg, 2008, p. 357.

7 *Nanostructured Materials for Advanced Technological Applications*, ed. J. P. Reithmaier, P. Petkov, W. Kulisch and C. Popov, Springer, Netherlands, 2009, p. 547.

8 L. Kharghanian and A. Moghimi, *Asian J. Chem.*, 2013, **25**, 5904–5906.

9 *Nanostructured Semiconductors: From Basic Research to Applications*, ed. P. Granitzer and K. Rumpf, CRC Press, New York, 2014, p. 700.

10 *Metal Chalcogenide Nanostructures for Renewable Energy Applications*, ed. A. Qurashi, Wiley, New York, 2015, p. 320.

11 A. P. Alivisatos, *Science*, 1996, **271**, 933–937.

12 N. N. Ledentsov, V. M. Ustinov, V. A. Shchukin, P. S. Kop'ev, Z. I. Alferov and D. Bimberg, *Semiconductors*, 1998, **32**, 343–365.

13 Z. I. Alferov, *Rev. Mod. Phys.*, 2001, **73**, 767–782.

14 C. Cui, X. Li, J. Liu, Y. Hou, Y. Zhao and G. Zhong, *Nanoscale Res. Lett.*, 2015, **10**, 431.

15 D. S. Wang, C. H. Hao, W. Zheng, Q. Peng, T. H. Wang, Z. M. Liao, D. P. Yu and Y. D. Li, *Adv. Mater.*, 2008, **20**, 2628–2632.

16 J. Yang, E. H. Sargent, S. O. Kelley and J. Y. Ying, *Nat. Mater.*, 2009, **8**, 683–689.

17 Z. H. Sun, Z. Yang, J. H. Zhou, M. H. Yeung, W. H. Ni, H. K. Wu and J. F. Wang, *Angew. Chem., Int. Ed.*, 2009, **48**, 2881–2885.

18 A. M. Smith, M. C. Mancini and S. Nie, *Nat. Nanotechnol.*, 2009, **4**, 710–711.

19 P. Jiang, Z.-Q. Tian, C.-N. Zhu, Z.-L. Zhang and D.-W. Pang, *Chem. Mater.*, 2012, **24**, 3–5.

20 X. Wang, H. Huang, B. Liang, Z. Liu, D. Chen and G. Shen, *Crit. Rev. Solid State Mater. Sci.*, 2013, **38**, 57–90.

21 X. Shi, S. Zheng, W. Gao, W. Wei, M. Chem, F. Deng, X. Liu and Q. Xiao, *J. Nanopart. Res.*, 2014, **16**, 2741.

22 S. Ummartyotin and Y. Infahsaeng, *Renewable Sustainable Energy Rev.*, 2015, **55**, 17–24.

23 N. Kaur, S. Kaur, J. Singh and M. Rawat, *J. Bioelectron. Nanotechnol.*, 2016, **1**, 1–5.

24 S. Goel, F. Chen and W. Cai, *Small*, 2014, **10**, 631–645.

25 J. Duan, H. Zhang, Q. Tang, B. He and L. Yu, *J. Mater. Chem. A*, 2015, **3**, 17497–17510.

26 R. C. Sharma and Y. A. Chang, *Bull. Alloy Phase Diagrams*, 1986, **7**, 263–269.

27 H. Reye and H. Schmalzried, *Z. Phys. Chem.*, 1981, **128**, 93–100.

28 C. Wagner, *J. Chem. Phys.*, 1953, **21**, 1819–1827.

29 H. Rau, *J. Phys. Chem. Solids*, 1974, **35**, 1553–1559.

30 G. Bonnecaze, A. Lichanot and S. Gromb, *J. Phys. Chem. Solids*, 1978, **39**, 299–310.

31 G. Bonnecaze, A. Lichanot and S. Gromb, *J. Phys. Chem. Solids*, 1978, **39**, 813–821.

32 A. V. Ditman and I. N. Kulikova, *Zh. Fizich. Khimii*, 1979, **53**, 260–261, in Russian.

33 K. Mitteilung, *Z. Phys. Chem.*, 1980, **119**, 251–255.

34 M. K. van Doorselaer, *J. Photogr. Sci.*, 1987, **35**, 42–52.

35 P. Junod, *Helv. Phys. Acta*, 1959, **32**, 567–600.

36 P. Junod, H. Hediger, B. Kilchör and J. Wullschleger, *Philos. Mag.*, 1977, **36**, 941–958.

37 S. H. Ehrlich, *J. Imaging Sci. Technol.*, 1993, **37**, 73–91.

38 S. Chang, Q. Li, X. Xiao, K. Y. Wong and T. Chen, *Energy Environ. Sci.*, 2012, **5**, 9444–9448.

39 W. P. Lim, Z. Zhang, H. Y. Low and W. S. Chin, *Angew. Chem., Int. Ed.*, 2004, **43**, 5685–5689.

40 J. Yang and J. Y. Ying, *Angew. Chem., Int. Ed.*, 2011, **50**, 4637–4643.

41 G. X. Zhu and Z. Xu, *J. Am. Chem. Soc.*, 2011, **133**, 148–157.

42 A. I. Kryukov, A. L. Stroyuk, N. N. Zin'chuk, A. V. Korzhak and S. Y. Kuchmii, *J. Mol. Catal. A: Chem.*, 2004, **221**, 209–221.

43 S. Shen, Y. Zhang, Y. Liu, L. Peng, X. Chen and Q. Wang, *Chem. Mater.*, 2012, **24**, 2407–2413.

44 T. B. Nasrallah, H. Dlala, M. Amlouk, S. Belgacem and J. C. Bernede, *Synth. Met.*, 2005, **151**, 225–230.

45 T.-Y. Hsu, H. Buhay and N. P. Murarka, in *Millimeter Optics*, ed. G. A. Tanton, SPIE Proc., 1980, vol. 259, pp. 38–45.

46 D. Karashanova, D. Nihtianova, K. Starbova and N. Starbov, *Solid State Ionics*, 2004, **171**, 269–275.

47 L. Liu, S. Hu, Y.-P. Dou, T. Liu, J. Lin and Y. Wang, *Beilstein J. Nanotechnol.*, 2015, **6**, 1781–1787.

48 C. H. Liang, K. Terabe, T. Hasegawa and M. Aono, *Nanotechnology*, 2007, **18**, 485202.

49 Z. Xu, Y. Bando, W. Wang, X. Bai and D. Golberg, *ACS Nano*, 2010, **4**, 2515–2522.

50 A. N. Belov, O. V. Pyatilova and M. I. Vorobiev, *Adv. Nanopart.*, 2014, **3**, 1–4.

51 M. M. El-Nahass, A. A. M. Farag, E. M. Ibrahim and S. Abd-El-Rahman, *Vacuum*, 2004, **72**, 453–460.

52 U. M. Jadhav, S. N. Patel and R. S. Patil, *Res. J. Chem. Sci.*, 2013, **3**, 69–74.

53 P. Leidinger, R. Popescu, D. Gerthsen and C. Feldmann, *Chem. Mater.*, 2013, **25**, 4173–4180.

54 M. L. Pang, J. Y. Hu and H. C. Zeng, *J. Am. Chem. Soc.*, 2010, **132**, 10771–10785.

55 S. Xiong, B. Xi, K. Zhang, Y. Chen, J. Jiang, J. Hu and H. C. Zeng, *Sci. Rep.*, 2013, **3**, 2177.

56 P. Jiang, C.-N. Zhu, Z.-L. Zhang, Z.-Q. Tian and D.-W. Pang, *Biomaterials*, 2012, **33**, 5130–5135.

57 C. Li, Y. Zhang, M. Wang, Y. Zhang, G. Chen, L. Li, D. Wu and Q. Wang, *Biomaterials*, 2014, **35**, 393–400.

58 C. Xiao, J. Xu, K. Li, J. Feng, J. Yang and Y. Xie, *J. Am. Chem. Soc.*, 2012, **134**, 4287–4293.

59 X. Zhang and L.-D. Zhao, *J. Materiomics*, 2015, **1**, 92–105.

60 M. Adelifard and R. Torkamani, *J. Mater. Sci.: Mater. Electron.*, 2015, **26**, 7554–7563.

61 Y. Zhao, C. Rinzler and A. Allanore, *ECS J. Solid State Sci. Technol.*, 2017, **6**, 3010–3016.

62 S. Kashida, N. Watanabe, T. Hasegawa, H. Iida, M. Mori and S. Savrasov, *Solid State Ionics*, 2003, **158**, 167–175.

63 L. Zhu, Z. Meng, G. Trisha and W.-C. Oh, *Chin. J. Catal.*, 2012, **33**, 254–2604.

64 A. Pourahmad, *Superlattice Microst.*, 2012, **52**, 276–287.

65 J. Jang, K. Cho, S. H. Lee and S. Kim, *Mater. Lett.*, 2008, **62**, 1438–1440.

66 L. Han, Y. Lv, A. M. Asiri, A. O. Al-Youbi, B. Tu and D. Y. Zhao, *J. Mater. Chem.*, 2012, **22**, 7274–7279.

67 S. I. Sadovnikov and A. A. Rempel, *Neorg. Mater.*, 2015, **51**, 829–837; *Inorg. Mater.*, 2015, **51**, 759–766, in Russian.

68 S. I. Sadovnikov, A. I. Gusev, E. Yu. Gerasimov and A. A. Rempel, *Chem. Phys. Lett.*, 2015, **642**, 17–21.

69 R. Chen, N. T. Nuhfer, L. Moussa, H. R. Morris and P. M. Whitmore, *Nanotechnology*, 2008, **19**, 455604.

70 W. Zhang, L. Zhang, Z. Hui, X. Zhang and Y. Qian, *Solid State Ionics*, 2000, **130**, 111–114.

71 X. F. Qian, J. Yin, J. C. Huang, Y. F. Yang, X. X. Guo and Z. K. Zhu, *Mater. Chem. Phys.*, 2001, **68**, 95–97.

72 X. F. Qian, J. Yin, S. Feng, S. H. Liu and Z. K. Zhu, *J. Mater. Chem.*, 2001, **11**, 2504–2506.

73 C. Xu, Z. Zhang and Q. Ye, *Mater. Lett.*, 2004, **58**, 1671–1676.

74 X. Lu, L. Li, W. Zhang and C. Wang, *Nanotechnology*, 2005, **16**, 2233–2237.

75 V. B. Prabhune, N. S. Shinde and V. J. Fulari, *Appl. Surf. Sci.*, 2008, **255**, 1819–1823.

76 H. Meherzi-Maghraoui, M. Dachraoui, S. Belgacem, K. D. Buhre, R. Kunst, P. Cowache and D. Lincot, *Thin Solid Films*, 1996, **288**, 217–223.

77 H. Li, J. X. Li, G. D. Li, D. P. Liu and J. S. Chen, *Chem.–Eur. J.*, 2007, **13**, 8754–8761.

78 S. S. Dhumure and C. D. Lokhande, *Mater. Chem. Phys.*, 1991, **28**, 141–144.

79 L.-M. Lyu and M. H. Huang, *Chem.–Asian J.*, 2013, **8**, 1847–1853.

80 M. Lismont, C. A. Paez and L. Dreesen, *J. Colloid Interface Sci.*, 2015, **447**, 40–49.

81 Z. Li, L. Jia, Y. Li, T. He and X.-M. Li, *Appl. Surf. Sci.*, 2015, **345**, 122–126.

82 X. Peng, M. C. Schlamp, A. V. Kadavanich and A. P. Alivisatos, *J. Am. Chem. Soc.*, 1997, **119**, 7019–7029.

83 F. Pinaud, D. King, H. P. Moore and S. Weiss, *J. Am. Chem. Soc.*, 2004, **126**, 6115–6123.

84 G. Hota, S. Jain and K. C. Khilara, *Colloids Surf., A*, 2004, **232**, 119–127.

85 D. O. Demchenko, R. D. Robinson, B. Sadtler, C. K. Erdonmez, A. P. Alivisatos and L.-W. Wang, *ACS Nano*, 2008, **2**, 627–636.

86 A. Emamdoust, S. F. Shayesteh and M. Marandi, *Pramana*, 2013, **80**, 713–721.

87 D. Gerion, F. Pinaud, S. C. Williams, W. J. Parak, D. Zanchet, S. Weiss and A. P. Alivisatos, *J. Phys. Chem. B*, 2001, **105**, 8861–8871.

88 X. Gao, Y. Cui, R. M. Levenson, L. W. K. Chung and S. Nie, *Nat. Biotechnol.*, 2004, **22**, 969–976.

89 N. Tipcompor, S. Thongtem and T. Thongtem, *J. Nanomater. (Hindawi)*, 2013, **2013**, 970489.

90 J. Xiang, H. Cao, Q. Wu, S. Zhang, X. Zhang and A. A. R. Watt, *J. Phys. Chem. C*, 2008, **112**, 3580–3584.

91 Y. Yu, K. Zhang and S. Sun, *Appl. Surf. Sci.*, 2012, **258**, 7181–7187.

92 D. Deng, J. Xia, J. Cao, L. Qu, J. Tian, Z. Qian, Y. Gu and Z. Gu, *J. Colloid Interface Sci.*, 2012, **367**, 234–240.

93 M. S. Sadjadi and A. Khalilzadegan, *Journal of Non-Oxide Glasses*, 2015, **7**, 55–63.

94 J. Zeng, Y. Zheng, M. Rycenga, J. Tao, Z. Y. Li, Q. Zhang, Y. Zhu and Y. Xia, *J. Am. Chem. Soc.*, 2010, **132**, 8552–8853.

95 L. Gutierrez, C. Aubry, M. Cornejo and J.-P. Croue, *Langmuir*, 2015, **31**, 8865–8872.

96 S. d'Souza, P. Mashazi, J. Britton and T. Nyokong, *Polyhedron*, 2015, **99**, 112–121.

97 D. Philip, *Spectrochim. Acta, Part A*, 2010, **75**, 1078–1081.

98 R. Mendoza-Reséndez, A. Gómez-Treviño, E. D. Barriga-Castro, N. O. Núñez and C. Luna, *RSC Adv.*, 2014, **4**, 1650–1658.

99 D. Ayodhya and G. Veerabhadram, *J. Photochem. Photobiol., B*, 2016, **157**, 57–69.

100 H.-Y. Yang, Y.-W. Zhao, Z.-Y. Zhang, H.-M. Xiong and S.-N. Yu, *Nanotechnology*, 2013, **24**, 055706.

101 A. C. C. Esteves and T. Trindade, *Curr. Opin. Solid State Mater. Sci.*, 2002, **6**, 347–353.

102 Q. Tang, S. M. Yoon, H. J. Yang, Y. Lee, H. J. Song, H. R. Byon and H. C. Choi, *Langmuir*, 2006, **22**, 2802–2805.

103 T. X. Wang, H. Xiao and Y. C. Zhang, *Mater. Lett.*, 2008, **62**, 3736–3738.

104 C. L. Zhang, S. M. Zhang, L. G. Yu and Z. J. Zhang, *Mater. Lett.*, 2012, **85**, 77–80.

105 C. Burda, X. B. Chen, R. Narayanan and E. I. Sayed, *Chem. Rev.*, 2005, **105**, 1025–1102.

106 Y. Zhao, D. W. Zhang and W. F. Shi, *Mater. Lett.*, 2007, **61**, 3232–3234.

107 C. G. Xu, Z. C. Zhang and Q. Ye, *Mater. Lett.*, 2004, **58**, 1671–1676.

108 M. H. Chen and L. Gao, *Mater. Lett.*, 2006, **60**, 1059–1062.

109 H. J. Zhai and H. S. Wang, *Mater. Res. Bull.*, 2008, **43**, 2354–2360.

110 X. B. Wang, W. M. Liu, J. C. Hao, X. G. Fu and B. S. Xu, *Chem. Lett.*, 2005, **34**, 1664–1665.

111 L. H. Dong, Y. Chu and Y. Liu, *J. Colloid Interface Sci.*, 2008, **317**, 485–492.

112 Y. Fang, C. Bai and Y. Zhang, *Chem. Commun.*, 2004, 804–805.

113 Y. Z. Sun and B. B. Zhou, *Mater. Lett.*, 2010, **64**, 1347–1349.

114 Z. Zhuang, Q. Peng, X. Wang and Y. Li, *Angew. Chem., Int. Ed.*, 2007, **46**, 8174–8177.

115 R. G. Chaudhuri and S. Paria, *J. Colloid Interface Sci.*, 2012, **369**, 117–122.

116 M. Y. Liu, Z. L. Xu, B. N. Li and C. M. Lin, *Mater. Lett.*, 2011, **65**, 555–558.

117 L. Y. Lv and H. Wang, *Mater. Lett.*, 2014, **121**, 105–108.

118 S. I. Sadovnikov, A. I. Gusev and A. A. Rempel, *Superlattice Microst.*, 2015, **83**, 35–47.

119 M. H. Huang, Y. Wu, H. Feick, N. Tran, E. Weber and P. Yang, *Adv.Mater.*, 2001, **13**, 113–117.

120 D. Wang, C. Hao, W. Zheng, Q. Peng, T. Wang, Z. Liao, D. Yus and Y. Li, *Adv. Mater.*, 2008, **20**, 2628–2632.

121 X. Wen, S. Wang, Y. Xie, X.-Y. Li and S. Yang, *J. Phys. Chem. B*, 2005, **109**, 10100–10106.

122 C. H. Liang, K. Terabe, T. Hasegawa, R. Negishi, T. Tamura and M. Aono, *Small*, 2005, **1**, 971–975.

123 S. C. Yan, H. T. Wang, Y. P. Zhang, S. C. Li and Z. D. Xiao, *J. Non-Cryst. Solids*, 2008, **354**, 5559–5562.
124 S. Yan, K. Shen, X. Xu, Y. Shi, J. Wu and Z. Xiao, *Synth. Met.*, 2011, **161**, 1646–1650.
125 C.-S. Tan, C.-H. Hsiao, S.-C. Wang, P.-H. Liu, M.-Y. Lu, M. H. Huang, H. Ouyang and L.-J. Chen, *ACS Nano*, 2014, **8**, 9422–9426.
126 M. Yarema, S. Pichler, M. Sytnyk, R. Seyrkammer, R. T. Lechner, G. Fritz-Popovski, D. Jarzab, K. Szendrei, R. Resel, O. Korovyanko, M. A. Loi, O. Paris, G. Hesser and W. Heiss, *ACS Nano*, 2011, **5**, 3758–3765.
127 Y. Du, B. Xu, T. Fu, M. Cai, F. Li, Y. Zhang and Q. Wang, *J. Am. Chem. Soc.*, 2010, **132**, 1470–1471.
128 W. Cai, D. W. Shin, K. Chen, O. Gheysens, Q. Cao, S. X. Wang, S. S. Gambhir and X. Chen, *Nano Lett.*, 2006, **6**, 669–676.
129 J. Chen, T. Zhang, L. L. Feng, M. Zhang, X. Zhang, H. Su and D. Cui, *Mater. Lett.*, 2013, **96**, 224–227.
130 C. Siva, C. N. Iswarya, P. Baraneedharan and M. Sivakumar, *Mater. Lett.*, 2014, **134**, 56–59.
131 X. M. Hou, X. L. Zhang, W. Yang and Y. Liu, *Mater. Res. Bull.*, 2012, **47**, 2579–2583.
132 M. Shakouri-Arani and M. Salavati-Niasari, *Spectrochim. Acta, Part A*, 2014, **133**, 463–471.
133 X. Wang, J. Zhuang, Q. Peng and Y. D. Li, *Nature*, 2005, **437**, 121–124.
134 Y. Zhang, G. Hong, Y. Zhang, G. Chen, F. Li, H. Dai and Q. Wang, *ACS Nano*, 2012, **6**, 3695–3702.
135 I. Hocaoglu, M. N. Çizmeciyan, R. Erdem, C. Ozen, A. Kurt, A. Sennaroglu and H. Y. Acar, *J. Mater. Chem.*, 2012, **22**, 14574–14681.
136 S. I. Sadovnikov and A. I. Gusev, *Eur. J. Inorg. Chem.*, 2016, **2016**, 4944–4957.
137 C. S. Sunandana, *Introduction to Solid State Ionics: Phenomenology and Applications*, CRC Press, Baton Rouge, 2015, p. 529.
138 J. Yang and H. Liu, *Metal-Based Composite Nanomaterials*, Springer, Berlin, Heidelberg, 2015, p. 259.
139 T. V. Vinogradova, I. A. Glukhova, L. N. Maskaeva and V. F. Markov, *Eur. Rev. Chem. Res.*, 2016, **10**, 122–129.
140 P. Anastas and N. Eghbali, *Chem. Soc. Rev.*, 2010, **39**, 301–312.
141 P. Patnaik, *Dean's Analytical Chemistry Handbook*, McGraw-Hill, New York, 2nd edn, 2004, Table 4.2, p. 1280.
142 P. C. Lee and D. Meisel, *J. Phys. Chem.*, 1982, **86**, 3391–3395.
143 S. I. Sadovnikov and A. A. Rempel, Patent No. 2572421 of Russian Federation, 2016, pp. 1–4.
144 S. I. Sadovnikov, Y. V. Kuznetsova and A. A. Rempel, *Nano-Structures & Nano-Objects*, 2016, **7**, 81–91.
145 Y. Zhang, Y. Liu, C. Li, X. Chen and Q. Wang, *J. Phys. Chem. C*, 2014, **118**, 4918–4923.
146 S. I. Sadovnikov, Y. V. Kuznetsova, A. I. Gusev and A. A. Rempel, Patent No. 2600761 of Russian Federation, 2016, pp. 1–11.
147 S. I. Sadovnikov, A. I. Gusev, E. Y. Gerasimov and A. A. Rempel, *Neorg. Mater.*, 2016, **52**, 487–492; *Inorg. Mater.*, 2016, **52**, 441–446, in Russian.
148 S. I. Sadovnikov, A. I. Gusev and A. A. Rempel, *Phys. Chem. Chem. Phys.*, 2015, **17**, 12466–12471.
149 S. I. Sadovnikov, A. I. Gusev and A. A. Rempel, Patent No. 2603666 of Russian Federation, 2016, pp. 1–13.
150 A. J. Frueh, *Z. Kristallogr.*, 1958, **110**, 136–144.
151 L. S. Ramsdell, *Am. Mineral.*, 1943, **28**, 401–425.
152 P. Rahlfs, *Z. Phys. Chem. B*, 1936, **31**, 157–194.
153 R. Sadanaga and S. Sueno, *Mineral. J.*, 1967, **5**, 124–148.
154 R. J. Cava, F. Reidinger and B. J. Wuensch, *J. Solid State Chem.*, 1980, **31**, 69–80.
155 T. Blanton, S. Misture, N. Dontula and S. Zdzieszynski, *Powder Diffr.*, 2011, **26**, 110–118.
156 C. Wang, X. Zhang, X. Qian, W. Wang and Y. Qian, *Mater. Res. Bull.*, 1998, **33**, 1083–1086.
157 V. Krylova and L. Samuolaitiene, *Mater. Sci.*, 2013, **19**, 10–14.
158 L. Grocholl, J. Wang and E. G. Gillan, *Mater. Res. Bull.*, 2003, **38**, 213–220.
159 B. Kim, C.-S. Park, M. Murayama and M. F. Hochella, *Environ. Sci. Technol.*, 2010, **44**, 7509–7514.
160 G. A. Martínez-Castañón, M. G. Sánchez-Loredo, H. J. Dorantes, J. R. Martínez-Mendoza, G. Ortega-Zarzosa and F. Ruiz, *Mater. Lett.*, 2005, **59**, 529–534.
161 L. V. Trandafilović, V. Djoković, N. Bibić, M. K. Georges and T. Radhakrishnan, *Mater. Lett.*, 2010, **64**, 1123–1126.
162 S. I. Sadovnikov, A. I. Gusev and A. A. Rempel, *Phys. Chem. Chem. Phys.*, 2015, **17**, 20495–20501.
163 S. I. Sadovnikov, A. I. Gusev and A. A. Rempel, *Rev. Adv. Mater. Sci.*, 2015, **41**, 7–19.
164 S. I. Sadovnikov, A. I. Gusev and A. A. Rempel, *Dokl. Akad. Nauk*, 2015, **464**, 568–573; *Dokl. Phys. Chem.*, 2015, **464**, 238–243, in Russian.
165 S. I. Sadovnikov, A. V. Chukin, A. A. Rempel and A. I. Gusev, *Fiz. Tverd. Tela*, 2016, **58**, 32–38; *Phys. Solid State*, 2016, **58**, 30–36, in Russian.
166 S. I. Sadovnikov, A. I. Gusev, A. V. Chukin and A. A. Rempel, *Phys. Chem. Chem. Phys.*, 2016, **18**, 4617–4626.
167 C. M. Perrott and N. H. Fletcher, *J. Chem. Phys.*, 1969, **50**, 2344–2350.
168 W. T. Thompson and S. N. Flengas, *Can. J. Chem.*, 1971, **49**, 1550–1563.
169 H. Okazaki and A. Takano, *Z. Naturforsch.*, 1985, **40**, 986–988.
170 F. Grønvold and E. F. Westrum, *J. Chem. Thermodyn.*, 1986, **18**, 381–401.
171 https://summary.ccdc.cam.ac.uk/structure-summary?ccdc=1062400.
172 A. J. Frueh, *Am. Mineral.*, 1961, **46**, 654–660.
173 A. I. Gusev, S. I. Sadovnikov, A. V. Chukin and A. A. Rempel, *Fiz. Tverd. Tela*, 2016, **58**, 246–251; *Phys. Solid State*, 2016, **58**, 251–257, in Russian.
174 K. Honma and K. Iida, *J. Phys. Soc. Jpn.*, 1987, **56**, 828–1836.
175 S. I. Sadovnikov and A. I. Gusev, *Phys. Solid State*, 2017, **59**, 1863–1870.
176 S. I. Sadovnikov and A. I. Gusev, *J. Alloys Compd.*, 2014, **610**, 196–202.

177 S. I. Sadovnikov and A. I. Gusev, *Fiz. Tverd. Tela*, 2014, **56**, 2274–2278; *Phys. Solid State*, 2014, **56**, 2353–2358, in Russian.

178 A. I. Gusev and A. A. Rempel, *Nanocrystalline Materials, Cambridge Intern*, Science Publ., Cambridge, 2004, p. 351.

179 Y. I. Petrov, *Physics of Small Particles*, Nauka, Moscow, 1982, p. 360, in Russian.

180 E. W. Montrol, *J. Chem. Phys.*, 1950, **18**, 183–185.

181 K. Terabe, T. Hasegawa, T. Nakayama and M. Aono, *Nature*, 2005, **433**, 47–50.

182 B. G. Kumar, B. Srinivas, M. D. Prasad and K. Muralidharan, *J. Nanopart. Res.*, 2015, **17**, 325.

183 B. Liu and Z. Ma, *Small*, 2011, **7**, 1587–1592.

184 C. Marambio-Jones and E. M. V. Hoek, *J. Nanopart. Res.*, 2010, **12**, 1531–1551.

185 X. Ma, Y. Zhao, X. Jiang, W. Liu, S. Liu and Z. Tang, *ChemPhysChem*, 2012, **13**, 2531–2535.

186 R. Costi, A. E. Saunders and U. Banin, *Angew. Chem., Int. Ed.*, 2010, **49**, 4878–4897.

187 N. Mishra, J. Lian, S. Chakrabortty, M. Lin and Y. Chan, *Chem. Mater.*, 2012, **24**, 2040–2046.

188 S. K. Dutta, S. K. Mehetor and N. Pradhan, *J. Phys. Chem. Lett.*, 2015, **6**, 936–944.

189 J. Yang and J. Y. Ying, *Chem. Commun.*, 2009, 3187–3189.

190 J. Yang, J. Y. Lee and J. Y. Ying, *Chem. Soc. Rev.*, 2011, **40**, 1672–1696.

191 R. D. Robinson, B. Sadtler, D. O. Demchenko, C. K. Erdonmez, L. W. Wang and A. P. Alivisatos, *Science*, 2007, **317**, 355–358.

192 S. Shen, Y. Zhang, L. Peng, Y. Du and Q. Wang, *Angew. Chem., Int. Ed.*, 2011, **50**, 7115–7118.

193 H. Zhang, M. Chen, D. M. Wang, L. Xu and X. D. Liu, *Opt. Mater. Express*, 2016, **6**, 2573–2583.

194 D. Wang, L. Liu, Y. Kim, Z. Huang, D. Pantel, D. Hesse and M. Alexe, *Appl. Phys. Lett.*, 2011, **98**, 243109.

195 S. Kaeriyama, T. Sakamoto, H. Sunamura, M. Mizuno, H. Kawaura, T. Hasegawa, K. Terabe, T. Nakayama and M. Aono, *IEEE J. Solid-State Circuits*, 2005, **40**, 168–186.

196 A. Nayak, T. Tamura, T. Tsuruoka, K. Terabe, S. Hosaka, T. Hasegawa and M. Aono, *J. Phys. Chem. Lett.*, 2010, **1**, 604–608.

197 H. Tanaka, T. Akai, D. Tanaka and T. Ogawa, *e-J. Surf. Sci. Nanotechnol.*, 2014, **12**, 185–188.

198 A. Gubicza, D. Z. Manrique, L. Pósa, C. J. Lambert, G. Mihály, M. Csontos and A. Halbritter, *Sci. Rep.*, 2016, **6**, 30775.

199 M. Morales-Masis, S. J. Molen, W. T. Fu, M. B. Hesselberth and J. M. Ruitenbeek, *Nanotechnology*, 2009, **20**, 095710.

200 S. I. Sadovnikov and A. I. Gusev, *J. Nanopart. Res.*, 2016, **18**, 277.

201 A. I. Gusev and S. I. Sadovnikov, *Fiz. Tekh. Poluprovodn.*, 2016, **50**, 694–699; *Semiconductors*, 2016, **50**, 682–687, in Russian.

202 A. I. Gusev and S. I. Sadovnikov, *Mater. Lett.*, 2017, **188**, 351–354.

203 S. I. Sadovnikov and A. I. Gusev, *Biointerface Res. Appl. Chem.*, 2016, **6**, 1797–1804.

204 Y. I. Kharkats, *Fiz. Tverd. Tela*, 1981, **23**, 2190–2192, in Russian.

205 Y. Y. Gurevich and Y. I. Kharkats, *Usp. Fiz. Nauk*, 1982, **136**, 693–728; *Phys.-Usp.*, 1982, **25**, 257–276, in Russian.

206 A. Henglein, *Ber. Bunsenges. Phys. Chem.*, 1997, **101**, 1562–1572.

207 Y. A. Krutyakov, A. A. Kudrinskiy, A. Y. Olenin and G. V. Lisichkin, *Usp. Khim.*, 2008, **77**, 242–269; *Russ. Chem. Rev.*, 2008, **77**, 233–257, in Russian.

208 M. Hu, J. Y. Chen, Z. Y. Li, L. Au, G. V. Hartland, X. D. Li, M. Marquez and Y. N. Xia, *Chem. Soc. Rev.*, 2006, **35**, 1084–1094.

209 S. P. Song, Q. Yu, Y. He, Q. Huang, C. H. Fan and H. Y. Chen, *Chem. Soc. Rev.*, 2010, **39**, 4234–4243.

210 J. Yang and H. Liu, *Metal-Based Composite Nanomaterials*, Springer, Cham, Heidelberg, Dordrecht, London, 2015, ch. 4, pp. 93–114.